HOKKAIDO UNIVERSITY

Title	A study to develop a new wind estimation method to elucidate the general circulation of the Venus atmosphere
Author(s)	池川, 慎一
Citation	北海道大学. 博士(環境科学) 乙第6995号
Issue Date	2016-06-30
DOI	10.14943/doctoral.r6995
Doc URL	http://hdl.handle.net/2115/62654
Type	theses (doctoral)
File Information	Shinichi_Ikegawa.pdf

Instructions for use

Hokkaido University Collection of Scholarly and Academic Papers : HUSCAP

A study to develop a new wind estimation method to elucidate the general circulation of the Venus atmosphere

（金星大気大循環の解明に向けた新たな風速推定手法の開発に関する研究）

北海道大学大学院環境科学院

池川 慎一

Shinichi Ikegawa

Contents

abstract 4

1 Introduction 5

1.1 Basic characteristics of Venus's atmosphere . . . 5

1.2 Features of wind field . . . 7

1.3 Theoretical studies of super-rotation . . . 7

1.4 Estimation of winds by cloud tracking . . . 8

1.5 Uncertainties of error in CMVs . . . 10

1.6 Gloals and structure of this study . . . 11

2 Dataset 12

3 Cloud tracking method 14

3.1 Preprocessing . . . 14

3.2 Necessity to use multiple images . . . 16

3.3 Estimation using multiple image pairs . . . 17

3.4 Spatial moving average of cross-correlation surfaces (optional but used) . . . 25

3.5 Quality control . . . 26

3.6 Example of CMVs . . . 26

4 Precision and error evaluation 28

4.1 Statistical precision evaluation . . . 28

4.2 Error evaluation by comparing CMVs . . . 31

4.3 Results . . . 37

4.4 Sensitivity to the template size or to the scale of tracked features . . . 43

5 Features of CMVs and comparison with previous studies 45

6 Summary and conclusions 50

A Estimation of the effective degrees of freedom **52**

B Elliptic paraboloid and parabola fitting **54**

B.1 Elliptic paraboloid fitting (two-dimensional) 54

B.2 Quadratic function (one-dimensional) 55

C Sensitivity experiment **56**

Acknowledgements **59**

Bibliography **59**

Abstract

Venus is covered with thick clouds of sulfuric acid that are present at 45–70 km above its surface. The winds on Venus are faster than the planet's rotation at all altitudes above its surface, in the same direction as its rotation. This phenomenon is known as super-rotation. In particular, at the cloud top level (65–70 km) of Venus, the winds reach up to 100 m s^{-1}, which is 60 times the speed of the planet's rotation at the equatorial region. One of the proposed mechanisms for the generation of super-rotation is the Gierasch mechanism, which has been supported by numerical simulations. In the Gierasch mechanism, super-rotation is generated by angular momentum transport in the poleward direction via meridional circulation and in the equatorward direction via eddies. To verify this mechanism, it is necessary to analyze the eddy transport of angular momentum on a horizontal scales of less than several thousand kilometers. However, previous studies have proven this to be a difficult task. The purpose of this study is to develop a method of cloud tracking and accuracy evaluation that is able to provide the datasets required to analyze this phenomenon on the horizontal scale. Here, the Venus Monitoring Camera onboard the European Space Agency's Venus Express, which captures UV images at 365 nm, is used for the cloud tracking. In the conventional cloud tracking methods, the cross-correlation coefficients between the sub-images of two images are computed, and cloud motion is estimated by selecting the maximum of the cross-correlation coefficients under the condition that the cloud morphology is advected by the wind. However, the estimation accuracy is reduced by noise and the time-evolving cloud morphology in the brightness image, etc. The cloud tracking method developed here resolves this problem by utilizing multiple images acquired simultaneously in a short time interval. The superposition improves the accuracy of wind velocity measurements and reduces false pattern matches that cause large errors by increasing the number of images. The improved results obtained in this study helped to clarify the Gierasch mechanism. In previous studies, a method of evaluating the accuracy of wind velocity measurements had not been established. Moreover, in several of these studies, the evaluation was performed based on the natural variability of the wind velocities. As a result, such evaluation methods are not suitable when the error is much smaller than the natural variability, because natural variability is regarded as part of the error. In dynamical studies, reliable error estimation in wind velocity is necessary at each grid point. In the present study, we developed evaluating (1) the precision in the wind measurements based on the lower confidence bound of cross-correlation and (2) the error in each wind measurement based on the two estimates of wind measurement. In (2), multiple

images obtained during an orbit can be used to estimate the error by subdividing them into two groups, performing cloud tracking for each group, and comparing the results. The statistical error was obtained from screening using the two methods described above to evaluate the accuracy and error of each wind ($< 45°$ S) about 210–298 days and 436–530 days after the spacecraft entered the Venusian orbit on 20 April, 2006. At low latitudes, the median of accuracy obtained using method (1) was about 8 m s^{-1}, and the error obtained from comparing winds using method (2) was about 2 m s^{-1}. The error in the wind measurement, which was less than 10 m s^{-1}, was estimated by visually tracking clouds over successive images. Based on the results, we show that, using the winds derived by the proposed method, it will be possible to analyze physical phenomena taking place in less than several thousands of kilometers. The proposed method is now being applied to cloud tracking using the observation data of the Venus meteorological satellite, known as the Akatsuki orbiter, which was inserted into orbit on 7 December, 2015.

Chapter 1

Introduction

1.1 Basic characteristics of Venus's atmosphere

The surface gravity, mean density and diameter of Earth and Venus are roughly the same, and these two planets have been referred to as twins. However, as observational technology has advanced, it has been revealed that there are many characteristics that differ between Earth and Venus. For example, the period of rotation of Venus is much longer than that of Earth, at 243 days (e.g., *Shapiro et al.*, 1990; *Davies et al.*, 1992). Furthermore, the direction of rotation of Venus is westward, which is the opposite to that of Earth. Another characteristic of Venus is that its solar day is very long, at about 117 days. The environments close to the surface have also proved to differ greatly, with the atmospheric pressure at the surface of Venus being around 90 times that of Earth and the temperature about 2 times that of Earth (e.g., *Avduevskiy et al.*, 1983; *Seiff*, 1983; *Seiff et al.*, 1985).

	Diameter	Revolution period	Rotation period	Rotation direction	1 solar day	Surface atmos pressure	Surface temperature
Earth	6378 km	365 days	1 day	Eastward	1 day	1 bar	294 K
Venus	6050 km	224 days	243 days	Westward	117 days	92 bar	737 K

Table 1.1: Characteristics of Earth and Venus

At altitudes of around 45–70 km, there is a thick cloud layer above Venus (*Kliore and Patel*, 1980, 1982). Clouds that contain sulfuric acid droplets on Venus are divided into three classes. Sulfuric acid aerosols are composed of mode 1 (0.05–0.3 μm), mode 2 (0.9–1.4 μm) and mode 3 (2.5–4.5 μm) as in Fig. 1.1. As a result, upper and lower clouds can be observed at various wavelengths.

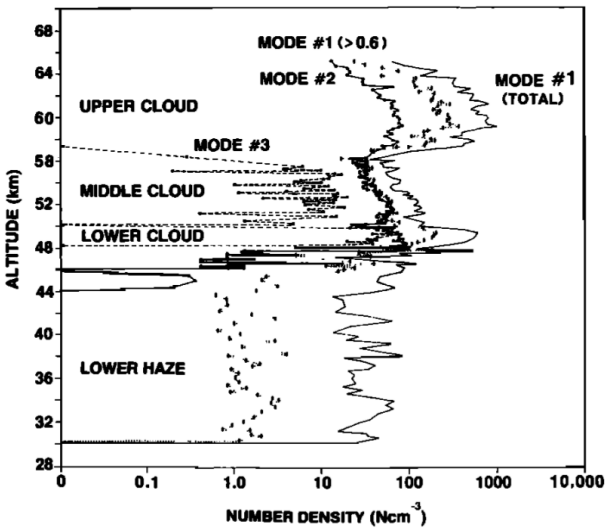

Figure 1.1: Vertical profile of density number for cloud droplets (*Knollenberg and Hunten*, 1980).

The albedo of Venus' atmosphere is 0.78, with most of the incoming sunlight reflected from the clouds (*Sobolev*, 1975). Cloud morphology obtained from using visible wavelengths in comparison to UV wavelengths has a smooth and uniform appearance (Fig. 1.2). However, at UV wavelengths, large-scale streaked structures and small-scale cell structures can be observed as in Fig. 1.2.

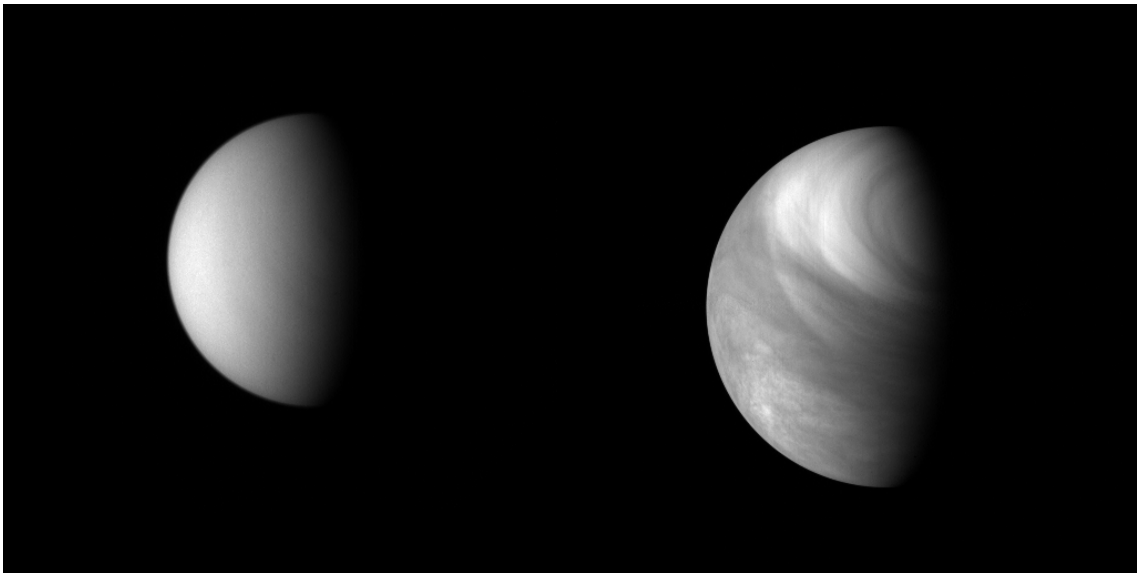

Figure 1.2: Images of Venus taken from the Venus Express, in visible (left) and ultraviolet (right) wavelengths.

1.2 Features of wind field

It was shown via ground-based observation[1] using UV wavelengths that the pattern of brightness on the equator of Venus has a period of 4 days (*Boyer and Guérin*, 1969). If this pattern is advected by the wind, then the wind close to the equator must be approximately 100 m s^{-1}. Observations by the Pioneer Venus and Venera series probes confirmed that at an altitude of 60 km, the westward wind is approximately 100 m s^{-1}. Furthermore, the westward wind increases gradually with altitude regardless of the location being observed (*Schubert et al.*, 1980). At altitudes below the cloud layer (∼45 km), the wind field is in close agreement with the solid body rotation (*Hunten*, 1983). This result was shown to be consistent with the wind field derived from temperature profiles assuming cyclostrophic balance (e.g., *Limaye et al.*, 1982). In recent research, it has been suggested, based on long-term observational data, that the short- and long-period zonal wind variation is dominated by Kelvin and Rossby waves (*Kouyama et al.*, 2013a; *Khatuntsev et al.*, 2013).

Turning our attention to meridional winds, it was discovered from observations on the dayside at the cloud top that there are slow winds from the equator towards the poles, with a maximum wind speed at the mid-latitudes of around 10 m s^{-1} (*Limaye and Suomi*, 1981). In addition, it has been reported that in the northern hemisphere at an altitude of 50 km, the speed of meridional winds is around 10 m s^{-1} poleward (*Carlson et al.*, 1991). Based on this information, it is possible that the flow from the equator toward the poles extends from 50 km to 70 km altitude. On the other hand, a recent research showed that the global meridional circulation on the nightside is slightly reversed in the lower cloud (*Hueso et al.*, 2015).

In regards to convergence and divergence on the dayside at the cloud top, there is a region of convergence at low latitudes, and a region of divergence close to the mid-latitudes (*Limaye*, 2007). However, both of these results are from cloud tracking of the brightness distribution on the dayside, and it remains unclear what kind of distribution the mean meridional flow forms.

1.3 Theoretical studies of super-rotation

Several generation mechanisms have been hypothesized for the super-rotation. Among these are the Gierasch mechanism (*Gierasch*, 1975) and theory of the thermal tides (*Fels and Lindzen*, 1974), which have both been supported by numerical simulations. The former is the theory that super-rotation is generated by the transport of angular momentum in an equatorward direction by large-scale eddies. The second theory states that, as a result of the diurnal tides propagates downward the surface, the momentum between the Venus atmosphere and the surface is exchanged. Therefore, the net momentum of the Venus atmosphere became weatward. In the research of *Fels and Lindzen* (1974), it was suggested that the thermal tides may break before reaching the surface. However, in recent studies using numerical simulations, it was found that the thermal tides do reach the surface (*Takagi and*

[1] At UV wavelengths, the dayside of the cloud top at an altitude of approximately 70 km can be observed (*Kawabata*, 1987).

Matsuda, 2007). This theory has yet to be confirmed by observational evidence.

Previous studies using numerical simulation[2] revealed that the horizontal eddies generated as a result of barotropic instability cause the transport of angular momentum toward the equator at the cloud top level (e.g., *Rossow and Williams*, 1979; *Iga and Matsuda*, 1999; *Matsuda*, 2000). However, no barotropic instability has been indicated in observations to date. There is a large gap between the theoretical research and observations.

On the other hand, in previous research on the existence of thermal tides, the structure of thermal tides obtained by superimposing cloud moving velocities (CMVs) on the dayside at cloud-top altitudes at solar-locked coordinates was in agreement with the structure obtained from numerical simulation (*Newman and Leovy*, 1992; *Takagi and Matsuda*, 2005). It was suggested that near the equator, a diurnal tide in which the zonal wind takes its minimum value at noon is predominant, while at mid-latitudes, a semidiurnal tide is predominant (e.g., *Newman and Leovy*, 1992; *Takagi and Matsuda*, 2005; *Limaye*, 2007; *Khatuntsev et al.*, 2013). Additionally, the meridional wind takes its maximum between 1 p.m. and 3 p.m. at southern latitudes around 50°S (e.g., *Newman and Leovy*, 1992; *Takagi and Matsuda*, 2005; *Limaye*, 2007; *Khatuntsev et al.*, 2013). Moreover, a semidiurnal tide with an amplitude of 5 K was detected from the retrieved temperature data on the nightside, estimated from infrared obtained by the Visible and Infrared Thermal Imaging Spectrometer onboard the Venus Express (VEX) (*Migliorini et al.*, 2012). These observational results support the numerical simulations.

1.4 Estimation of winds by cloud tracking

The gap between these observations and the theoretical/numerical results remains large. This is because both the vertical and horizontal coverage of cloud tracking is limited, but it is also because their spatial resolution and accuracy is limited or uncertain (note that, since large-scale horizontal wind disturbances are expected to have a "red" spectral feature from a dynamical perspective, the spatial resolutions have a limited accuracy). In previous studies, CMVs are estimated either by visually tracking clouds over successive images (manual tracking) or by computing cross-correlations between two images (digital tracking). Manual tracking generally performs better, but it is time consuming, and the obtained CMVs tend to be sparse. In digital tracking, the cross-correlation between the sub-images of two images is computed. To estimate the motion of cloud, the region for the sub-image from one of the two images is slid to maximize the correlation.

Figure. 1.3 shows the the cross sections of correlation surfaces as a function of distance, which are obtained by this cross-correlational method. These typical cross-correlation surfaces can be used as a criterion both in cases where it is easy to accurately estimate CMVs and where it is not. Figure. 1.3(a) shows a case where the cross section of the correlation surface is single peak, and there is only one candidate for the template destination.

[2] *Yamamoto and Takahashi* (2003a) and others succeeded in reproducing the super-rotation over all cloud layers. However, unrealistic solar heating was given as an initial condition in this study. There is no research that has succeeded in reproducing super-rotation over all cloud layers with more realistic conditions provided. Nevertheless, there is a great deal of research that succeeds in reproducing super-rotation in the cloud layer of Venus.

The cross section of the correlation surface in Fig. 1.3(b) has multiple peaks, and the template destination does not necessarily correspond to the maximum peak. Accordingly using a simple cross-correlationmethod, it gives erroneous CMVs because of mismatching between the sub-iamge patterns, as in Fig. 1.4(a). As a result, the zonal mean wind obtained from the wind field, which includes numerous erroneous CMVs, has little meaning.

In recent studies (*Kouyama et al.*, 2012, 2013a; *Ogohara et al.*, 2012), erroneous matches are corrected by comparing neighboring CMVs and, if the discrepancy exceeds a threshold, selecting secondary (or tertiary etc.) correlation peaks. The treatment significantly reduces the error as in Fig. 1.4(b), but it appears that the results are still not free from significant errors.

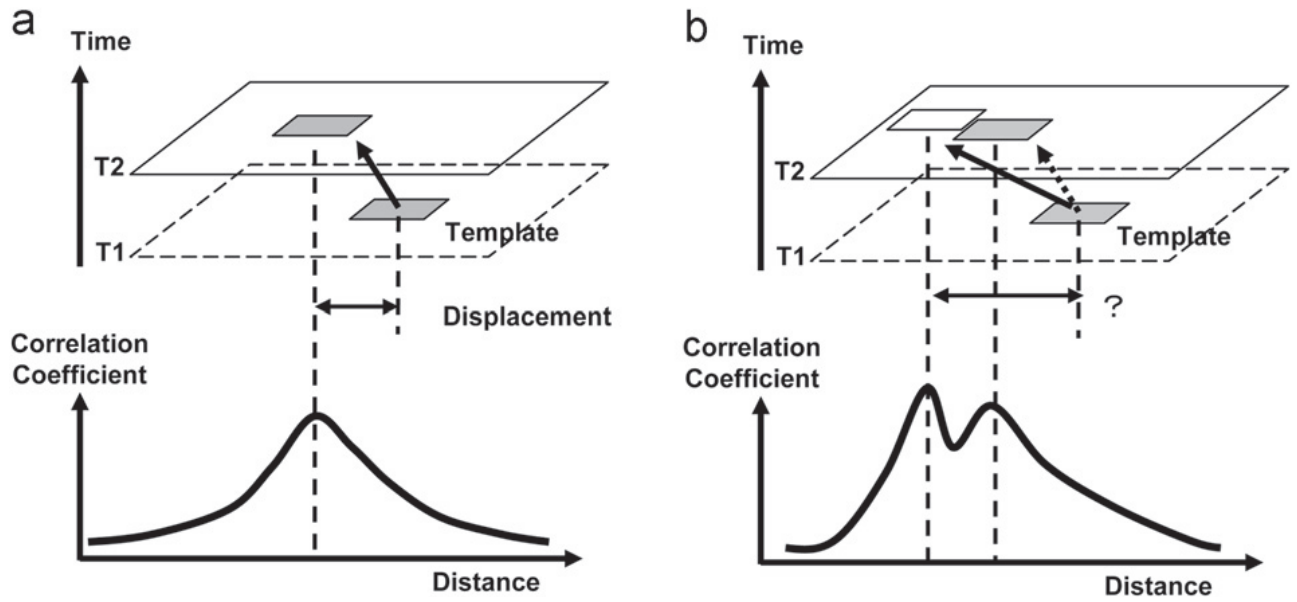

Figure 1.3: (a) Case with a single peak in the cross section of the spatial correlation surface: there is a one-to-one correspondence between the sub-image patterns at times T1 and at T2. (b) Case with multiple peaks in the cross section of the spatial correlation surface: the sub-image patterns at times T1 and T2 do not have a one-to-one correspondence (*Kouyama et al.*, 2012).

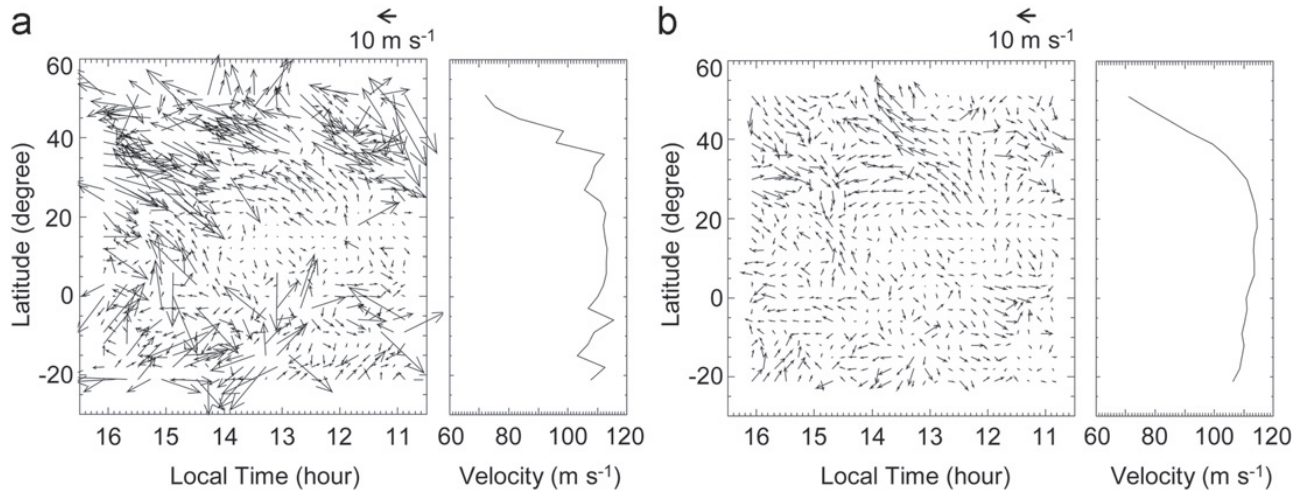

Figure 1.4: (a) Horizontal wind vector field obtained from the maxima of the cross-correlation surface, and the corresponding zonal mean zonal winds. (b) Horizontal wind vector field obtained after selecting a 2nd, 3rd $\cdots$ peak, having taken into account consistency with the surrounding wind vectors (*Kouyama et al.*, 2012).

1.5 Uncertainties of error in CMVs

In order to analyze the target physical phenomena, a level of accuracy above the minimum at which the phenomena can be resolved is required. Therefore, it is necessary to calculate values for the quality and accuracy of the CMVs at each grid point. Quality control schemes for the CMVs of Earth's atmosphere are made based on changes in the wind vector over successive time, and consistency with the spatially-adjacent wind vectors, and forecast and radiosonde data (*Holmlund*, 1998).

Many of the studies use the standard deviation (for example, by computing CMVs for each latitude and time, and then averaging over time) to quantify the uncertainties in CMVs estimates. However, not only measurement error but also natural variability contributes to the size of the standard deviation, so this measure is not very insightful when the error is much greater than the natural variability. If cloud tracking is to be improved to resolve the spatial features of cloud-top wind fields, a more elaborate measure of uncertainty is needed.

An obvious source of uncertainty in CMVs is the pixel discretization of the brightness measurement. An error in destination finding by one pixel causes a difference corresponding to the pixel size. This issue can be relaxed to some extent by conducting sub-pixel CMV determination (e.g, *Kouyama et al.*, 2012). On the other hand, there are sources of uncertainty that make it difficult to track clouds even at the original image resolution, such as pointing inaccuracy, noise, and (time-evolving) cloud morphology (see, e.g., *Moissl et al.*, 2009 for futher discussion). Especially, fuzzy low-contrast features typically found at mid and high latitudes are the serious source of uncertainty. Since the brightness morphology has a high spatial variability, it would be desirable not only to estimate the overall accuracy but also to evaluate it for each CMV individually.

The time interval suitable for cloud tracking is a few hours (*Rossow et al.*, 1990). For the Pioneer Venus and

Galileo, imaging observation was conducted with time intervals about 1 to 4 h. Thus, it is reasonable to conduct digital cloud tracking with a single pair of images. However, the television camera onboard the Mariner 10 and the Venus Monitoring Camera (VMC) onboard the VEX capture images much more frequently. As mentioned earlier, one of the issue with digital cloud tracking is erroneous matches. This problem might be alleviated if features are tracked across multiple images over a short time interval. Also, the use of multiple images might improve the accuracy of CMVs; superposition is a basic technique in signal processing for improving the signal-to-noise ratio (SNR).

We also propose two methods for evaluating the precision and error of each CMV. One of them provides a relative measure of the precision provided that the peak selection is correct, and it is applicable to the conventional digital tracking using a pair of images. The other method is a more direct measure of the errors, but it can only be applied when a sufficient number of images are used for one estimation. The two methods can be used together to screen CMVs.

1.6 Gloals and structure of this study

The purpose of the present study is to develop a cloud tracking technique in which physical phenomena on a scale below several thousand kilometers can be resolved, and a method for evaluatting the accuracy of this technique. With the cloud tracking technique used in this study, we estimate the CMVs using multiple images simultaneously. This results in a reduction in the probability of selecting the incorrect maxima of the correlation coefficient when estimating CMVs. The accuracy and reliability of the CMVs obtained with this method are then evaluated.

The rest of this paper is organized as follows. Section 2 gives a brief description of the datasets. Section 3 introduces our cloud tracking method and shows the result for an orbit of the VEX. Section 4 describes the error estimation methods and their statistics. Section 5 shows CMVs for multiple orbits and compares them with previous studies. Conclusions are drawn in Section 6.

Chapter 2

Dataset

We use the version 2.0 UV data of the VMC onboard the VEX. Features of the VEX spacecraft are described by *Markiewicz et al.* (2007). VEX was put into an elliptical polar orbit with a period of 24 h in April 2006. As shown in Fig. 2.1, its orbiter has a pericenter near the north pole and an apocenter near the south pole (*Markiewicz et al.*, 2007).

The VMC has four channels at 365, 513, 950, and 1010 nm (*Markiewicz et al.*, 2007). Each of the channels provides 16-bit images of 512×512 pixels. The wavelength of the UV channel, 365 nm, is the same as that of the Pioneer Venus Orbiter Cloud Photopolarimeter. The spatial resolution of the VMC images is 50 km/pixel at the sub-spacecraft point (SSP) when the spacecraft is at the apocenter. The observation is conducted when the spacecraft is in the ascending nodes; that is, when it is traveling from south to north.

We use the data having the resolution at SSP between 40 km and 21 km, which corresponds to the SSP latitude between 66°S and 47°S. The time it takes for the spacecraft to travel between these latitudes is approximately 4 h. The low latitude limit of 47°S is introduced so that the images used cover the full disk. The high latitude limit of 66°S is determined in terms of the travel time and latitudinal coverage.

Figure 2.2 shows the Local Time of the sub-spacecraft longitudes of Ascending Nodes (LTAN) where the spacecraft crosses the equator from the south.We define three periods according to LTAN: the periods 1 (days 29 to 72), 2 (days 210 to 298), and 3 (days 436 to 500). These periods are defined to have LTAN between 6 and 18 h. The longitudinal coverage of UV images is maximized when the LTAN is at around the local noon.

The detector of the camera was damaged by viewing the Sun during the cruise to Venus. As a result, the UV images suffer fixed pattern noise (*Titov et al.*, 2012). Although the noise was corrected by flattening (*Moissl et al.*, 2009), the correction is often insufficient for images taken with relatively large exposure time. In this study, we did not use images with the exposure time greater than 20 ms.

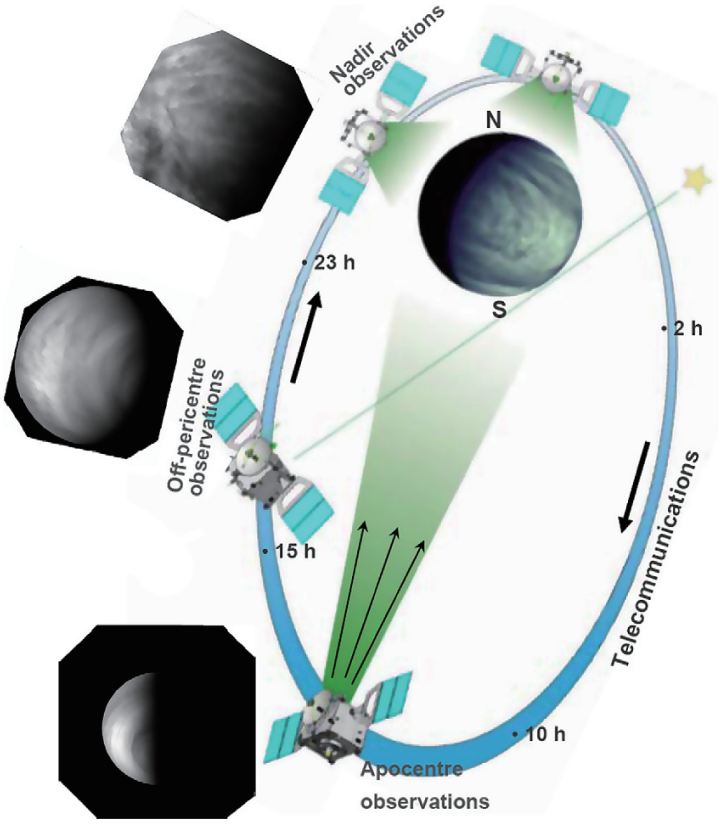

Figure 2.1: Overview of the VEX the orbit and telecommunications (*Titov et al.*, 2012).

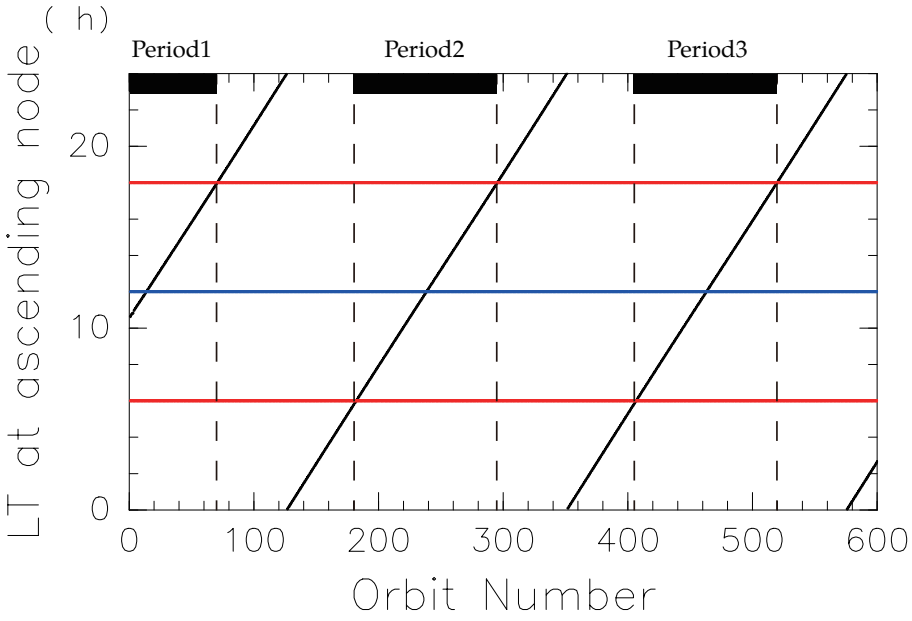

Figure 2.2: The LTAN of the VEX up to the orbit 600 (11, Dec, 2007). The red lines show 6 am and 18 pm, blue line shows the noon.

Chapter 3

Cloud tracking method

This section explores the problem of the conventional cloud tracking and introduces our cloud tracking method. It is demonstrated how it works and how it improves the digital tracking.

3.1 Preprocessing

Our method uses multiple images obtained over a few hours. The time interval does not have to be equal, but it should not be highly unequal. The VMC images are sampled every 20–40 min in many cases, but occasionally intense sampling with a few minute interval is conducted over a short period of time (say, 1 hour). To avoid highly unequal sampling, images are thinned out if the time interval is less than 10 min. The images often contain a few bad pixels. The values at the bad pixels are substituted by the mean values of the surrounding 8 pixels.

We apply the optical correction proposed by *Kouyama et al.* (2013b) and the limb fitting proposed by *Ogohara et al.* (2012) to the original image data. The optical correction corrects a small distortion in the images, and the limb fitting corrects the pointing angle of the spacecraft recorded in the Spacecraft Planet Instrument C-matrix Events (SPICE) metadata. To see the impact of the corrections, we make a brief comparison with the results obtained without the corrections (Section 4.3).

The cloud top height is assumed to be at 65 km from the mean planetary surface, which is at 6051.8 km from the center of Venus. The images were projected onto a longitude-latitude coordinate system by interpolating onto a regular grid with the interval of 0.125° both in longitude and latitude. This is oversampling, since the resolution of the original image is 0.2° at maximum. The oversampling is deliberately made to enable sub-pixel CMV determination.

The UV brightness depends on the solar zenith angle and the spacecraft zenith angle. We correct the dependences

by using the empirical formulation by *Belton et al.* (1991):

$$F = \frac{\pi\mu}{B(\mu\mu')^k}\frac{1-\exp(-\mu'/b)}{1-\exp(-\mu/a)}I \tag{3.1}$$

Here, F is the corrected brightness, I is the original UV brightness, μ' is the cosine of the solar zenith angle θ', μ is the cosine of the spacecraft zenith angle θ, and $B = 0.59$, $k = 0.90$, $a = 0.00547$, and $b = 0.0039$ are non-dimensional constants. These parameters were optimized for Galileo Solid-State Imaging's original image data at the violet wavelength of 418 nm, but it appears that they are not unreasonable for the present data. We do not use the brightness data where the solar zenith angle θ' is greater than 80°, since the correction with the Eq. (3.1) is not accurate enough for cloud tracking for such large θ'. We also exclude the data where the spacecraft zenith angle θ is greater than 75°, since the image pixels for such cases are highly elongated in the longitude-latitude coordinate system.

Figure 3.1 shows an example of the UV brightness data from the orbit 246. This orbit is used to demonstrate our method in this section. Figure 3.1a shows an original UV brightness image of the southern hemisphere taken at a distance of 48,000 km from the surface. The resolution at the sub-spacecraft point is 40 km. Figure 3.1b shows F obtained by the preprocess. Thus the regions where $\theta' > 80°$ or $\theta > 75°$ are masked (treated as data missing). This image is used as the first one to track clouds in the orbit 246, and the time, 01:00:31, is designated as t_0, which will be introduced later.

In some studies, high-pass filtering is applied to optically flattened images before conducting cloud tracking (e.g, *Rossow et al.*, 1990). We do not do it in the control case, but we test the effect of high-pass filtering in Section 4.4. Note that the calculation of cross-correlation includes the subtraction of mean values, so the cross-correlational method, which we use, inherently includes a high-pass filter by running mean.

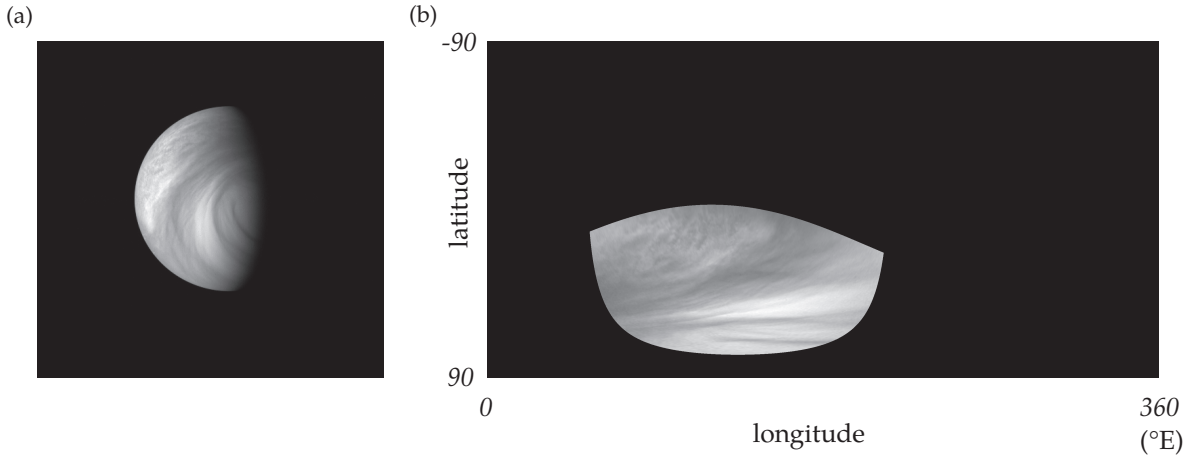

Figure 3.1: Example of the UV brightness data. (a) Original version 2.0 data at 01:00:31 UTC, 23 Dec, 2006 from the orbit 246. (b) As in (a) but for the preprocessed brightness F.

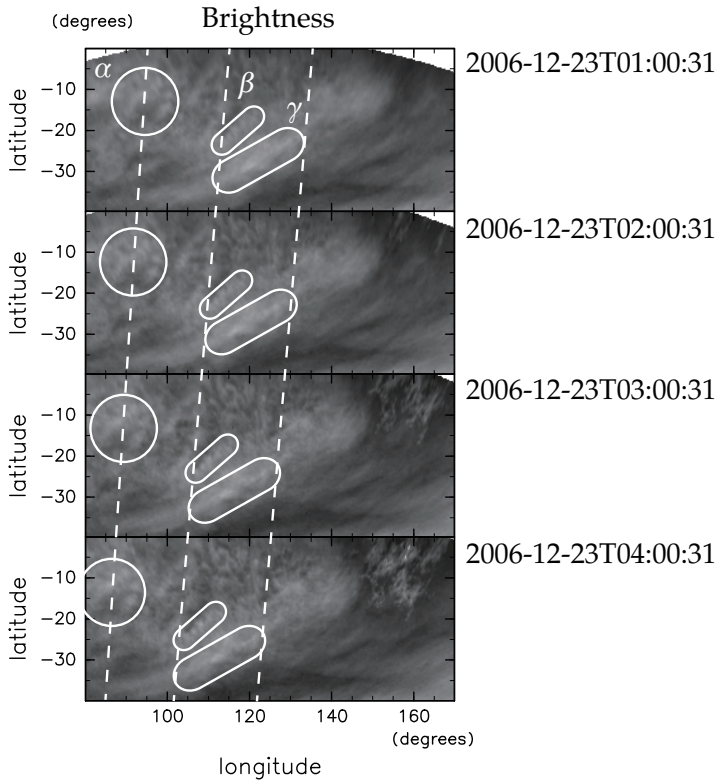

Figure 3.2: The preprocessed brightness F from the orbit 246, starting at 01:00 (as in Fig. 3.1) with one hour time interval. Dashed lines and solid enclosures highlights features that can be readily tracked by visual inspection.

3.2 Necessity to use multiple images

Figure 3.2 shows a time evolution of F at one hour interval. One can visually track patterns as indicated by dashed lines and solid enclosures. However, details of the patterns change with time. Thus the pattern match is more precise for shorter time intervals. However, the discretization error of velocity, expressed as $\Delta x/\Delta t$, where Δx is spacial resolution and Δt is time interval, is greater for smaller Δt. In the conventional digital cloud tracking by using a single pair of images, Δt has to be determined by considering this trade-off.

In the digital cloud tracking, cross-correlations are computed among sub-regions in preprocessed brightness data. Noise in images may shift the position where the maximum correlation occurs, causing error in wind estimation. Noise can also cause errors in pattern matching (false match). These effects are independent of Δt.

The digital cloud tracking by using two images relies on the "cross-correlation surfaces" like the ones shown in Fig. 3.3. For each of the two panels (a) and (b), a template region, $6^\circ \times 6^\circ$ in longitude and latitude, is specified in the preprocessed image at the earlier data. Cross-correlation is computed between F in this template region and that of a region with the same size in the image at the later time, which is called the target region. The target region is slid in this case with the $0.125^\circ \times 0.125^\circ$ interval over 28° both in longitude and latitude, and the result, called the cross-correlation surface, is shown two dimensionally in Fig. 3.3. In Fig. 3.3a, the cross-correlation has a

distinguished peak, which indicates the destination of the center of the target region. However, in Fig. 3.3b, there are multiple peaks that are comparable. Therefore, the destination is not identified uniquely. As will be shown later, the greatest peak actually corresponds to a false match. In the conventional digital cloud tracking, cases like Fig. 3.3b result in failure, which necessitates screening (e.g, *Rossow et al.*, 1990) or correction (e.g, *Kouyama et al.*, 2012; *Ogohara et al.*, 2012). Note that the effective degree of freedom to measure the confidence of cross-correlation is generally not equal to the number of sample members (in this case the number of pixels of the regions). The effective degrees of freedom estimated by Eq. (A.1) in Appendix A are 65 and 15 for Fig. 3.3a and 3.3b, respectively.

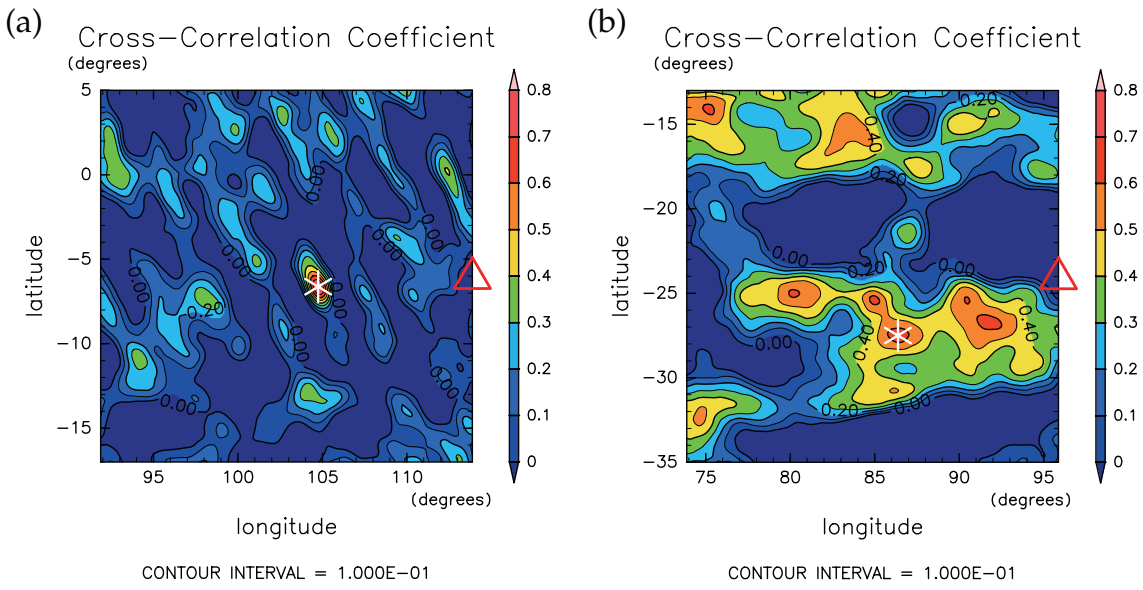

Figure 3.3: The cross-correlation coefficients calculated from two images separated by 200 min in the orbit 246. (a) A typical example where the cross-correlation has a distinguished maximum (denoted by the $*$ mark). The center of the template is at 114°E, 6°S (denoted by the $\triangle$ mark).The abscissa and the ordinate shows the longitude and latitude, respectively, of the center of the target regions. (b) As in (a) but for a typical example where the cross-correlation has multiple peaks that are comparable. The center of the template is at 96°E, 24°S. The cross-correlation is maximized when the center of the target is at the location designated by the $*$ mark.

3.3 Estimation using multiple image pairs

The problems that have been mentioned can be alleviated by superposing cross-correlations among multiple images taken successively at short time intervals. Superposition is widely used to increase SNR in signal processing. It is the case for the digital cloud tracking; superposition can increase the accuracy of cloud tracking, since the positional shift of the correlation maxima due to noise and the time variation of clouds is expected to be more or less random. Superposition is also effective to eliminate false peak match, as explained later.

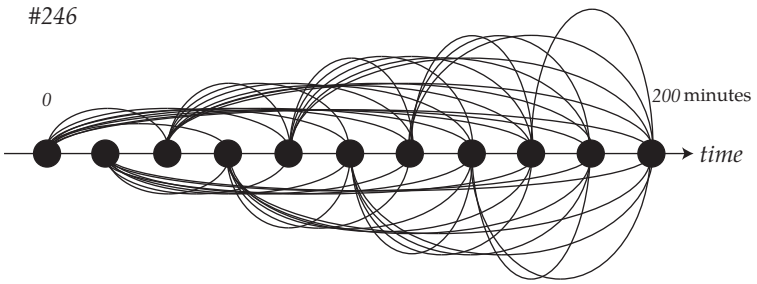

Figure 3.4: Example of the combinations of observation times to compute. Black circles show the observation times, which are at every 20 min in the orbit 246. The arcs show the combinations: on their left (earlier) ends are the times to set templates, and on their right (later) ends are the times to set targets.

We assume that the velocity of cloud feature movement is constant over the period to track clouds, $\Delta t_{\max}$, which is up to 3 h 40 min in this study; this limits is regulated by the limit on the SSP resolution described in Section 2. This assumption is to suppose a constant velocity in Lagrangian sense for each "air parcel". Observation times in the period are referred to as $t_0, t_1, \cdots, t_{K-1}$, where K is the number of the images used for estimation. As illustrated in Fig. 3.4, we use all of the combinations with time intervals greater than or equal to $\Delta t_{\min}$, which is set to 40 min in this study[1]. The number of the pairs used for the orbit 246 is 45.

The minimum time interval $\Delta t_{\min}$ is introduced because it is meaningless, though not harmful, to use pairs with very short time intervals. The discretization error $\Delta x/\Delta t_{\min}$ is 12 m s^{-1}, when $\Delta x = 30$ km and $\Delta t_{\min} = 40$ min. To further use the pairs with the shorter time interval of 20 min, for examples, does not contribute much to improve cloud tracking.

In this study, $\Delta t_{\max}$ is mainly determined by considering orbital factors. Without them, however, $\Delta t_{\max}$ should still be limited, since cloud features change with time. Also, the longer the time interval is, the greater is the chance for an air parcel on the dayside to be advected to the nightside, which makes tracking unavailable. Note that $\Delta x/\Delta t_{\max}$ is 2.1 m s^{-1}, when $\Delta x = 30$ km and $\Delta t_{\max}$ =3 h 40 min.

The size of the template region is set to 6° × 6° (48 × 48 grids), which corresponds to 640 × 640 km if at the equator (Fig. 3.5a). This template size is recommended by (*Kouyama et al.*, 2013a) based on a sensitivity test. The template regions is slid at every 3° both in longitude and latitude. Therefore, CMVs are obtained redundantly. We limited the latitudinal range to conduct cloud tracking to 10°N–60°S; the northern boundary is a consequence of the satellite orbit having the apocenter over the south pole, and the southern boundary is set because the estimated error tends to be greater at high latitude. We further limit our scope to 10°N–45°S when making statistics in Sections 4 and 5, since the CMVs obtained at further high latitude are very sparse. Sensitivity to the template size is examined in Section 4.4.

The search region is set to a window corresponding to zonal (eastward) velocities $u_{\min} = -200\frac{\cos\phi}{\cos 45°}$ m s^{-1} and $u_{\max} = 0$ m s^{-1}, and meridional (northward) velocities $v_{\max} = 70$ m s^{-1} and $v_{\min} = -70$ m s^{-1}. Here, ϕ is the

[1]The actual setting of $\Delta t_{\min}$ is 35 min to handle fluctuations in time intervals.

latitude of the center of the template; $u_{\min}$ is made a function of latitude to make the search region rectangular with respect to longitude and latitude (Fig. 3.5b).

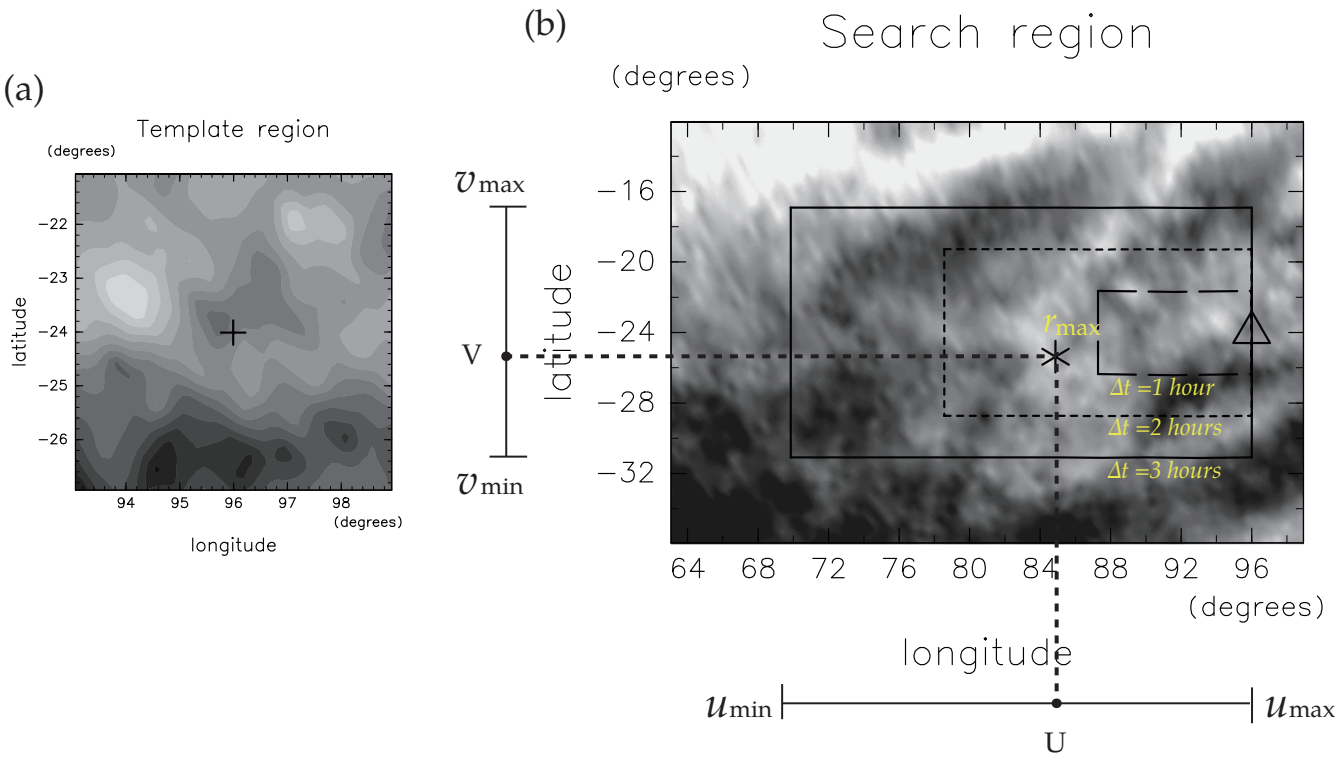

Figure 3.5: Example of template and search regions. (a) F in the template region whose center (designated by the + mark) is at 96°E, 24°S at 01:00:31 UTC, 23 Dec, 2006 in the orbit 246. (b) The search regions for Δt=1 hour (dotted rectangle), Δt=2 h (dash rectangle), and Δt=3 h (solid rectangle). The background image is F for $\Delta t \equiv 3$ h (at 04:00:31). The $*$ mark shows where the cross-correlation is maximized when $\Delta t = 3$ h, from which the cloud motion can be evaluated as indicated by the additional ordinate and abscissa.

The preprocessed brightness $F(\lambda, \phi, t)$, where λ, ϕ, and t are longitude, latitude, and time, respectively, is expressed discretely as

$$F_{a,b,n} = F(\lambda_a, \phi_b, t_n), \tag{3.2}$$

$$\lambda_a \equiv a\Delta\lambda \quad , \quad \phi_b \equiv b\Delta\phi, \tag{3.3}$$

where a and b are integers. Hereinafter grid points are specified as $[a, b]$. The observation times t_n ($n = 0, 1, \cdots, K-1$) are not necessarily equally spaced. The cross-correlation between the template whose center is at the grid point $[a, b]$ at t_n and the target whose center is at the grid point $[a + l, b + m]$ at t_{n+k} is

$$r^{n,n+k}_{a,b,l,m} = \frac{\sum_{i=-\frac{I}{2}}^{\frac{I}{2}-1}\sum_{j=-\frac{J}{2}}^{\frac{J}{2}-1}(F_{a+i,b+j,n}-\bar{F}_{a,b,n})(F_{a+l+i,b+m+j,n+k}-\bar{F}_{a+l+i,b+m+j,n+k})}{\sqrt{\sum_{i=-\frac{I}{2}}^{\frac{I}{2}-1}\sum_{j=-\frac{J}{2}}^{\frac{J}{2}-1}(F_{a+i,b+j,n}-\bar{F}_{a,b,n})^2}\sqrt{\sum_{i=-\frac{I}{2}}^{\frac{I}{2}-1}\sum_{j=-\frac{J}{2}}^{\frac{J}{2}-1}(F_{a+l+i,b+m+j,n+k}-\bar{F}_{a+l+i,b+m+j,n+k})^2}}, \quad (3.4)$$

$$\bar{F}_{a,b,n} \equiv \frac{1}{IJ}\sum_{i=-\frac{I}{2}}^{\frac{I}{2}-1}\sum_{j=-\frac{J}{2}}^{\frac{J}{2}-1}F_{a+i,b+j,n}. \quad (3.5)$$

Here, I and J are the pixel sizes in longitude and latitude ($I = J = 48$ in this study). The integer "distances" l and m correspond to the zonal and meridional velocities:

$$u^{n,n+k}_{l,b} = \frac{l\Delta\lambda R_c\cos\phi_b}{t_{n+k}-t_n}, \quad (3.6)$$

$$v^{n,n+k}_{m} = \frac{m\Delta\phi R_c}{t_{n+k}-t_n}, \quad (3.7)$$

where R_c is the distance from the planetary center to 65 km above the surface ($R_c = 6115.8$ km).

The ranges of l and m are set to cover the velocity ranges from $u_{\min}$ to $u_{\max}$ and from $v_{\min}$ to $v_{\max}$, respectively. In general, the longer the time interval $t_{n+k} - t_n$ is, the wider are the ranges of l and m.

The CMVs are defined at the grid points at t_0. For $t_n > t_0$, template positions have to be set by taking advection into account. This is done by introducing

$$r^{n,n+k}(\lambda_a,\phi_b,u^{n,n+k}_{l,b},v^{n,n+k}_{m}) \equiv r^{n,n+k}_{a+\Delta a,b+\Delta b,l,m}, \quad (3.8)$$

$$\Delta a \equiv \mathrm{round}\left[\frac{u^{n,n+k}_{l,b}(t_n-t_0)}{\Delta\lambda R_c\cos\phi_b}\right], \quad \Delta b \equiv \mathrm{round}\left[\frac{v^{n,n+k}_{m}(t_n-t_0)}{\Delta\phi R_c}\right], \quad (3.9)$$

where "round" is the round off function. Here, Δa and Δb represent respectively the longitudinal and latitudinal grid-point shifts corresponding to the advection over the time interval $t_n - t_0$ with the velocity $(u^{n,n+k}_{l,b}, v^{n,n+k}_{m})$. These offsets are necessary to have the template regions to be situated at the same location when the motion is traced back to the initial time t_0. In this study, we approximate $u^{n,n+k}_{l,b}$ and $v^{n,n+k}_{m}$ in Eq. (3.9) by $U \equiv -100$ m s^{-1} and 0 m s^{-1}, respectively, for simplicity, so

$$\Delta a = \mathrm{round}\left[\frac{U(t_n-t_0)}{\Delta\lambda R_c\cos\phi_b}\right], \quad \Delta b = 0. \quad (3.10)$$

This approximation causes the locations of the template regions not to agree at t_0. Therefore, it degrades the spatial resolution of CMV field. For example, if $\sqrt{(U-u_{l,b}^{n,n+k})^2+(V-v_{l,m}^{n,n+k})^2}=50$ m s^{-1}, the discrepancy between Eqs. (3.9) and(3.10) amounts to the difference of 360 km in length, when $t_n=t_0+2$ h. It corresponds to 3.4° if at the equator. Therefore, the degradation is not insignificant. However, it is minor if the spatial superposition described in Section 3.4 is conducted.

To track cloud features, cross-correlation maxima are searched by varying l and m for fixed n, k a, and b. Thus, we refer to the cross-correlation as a function of l and m as a cross-correlation surface. Figure 3.6a shows cross-correlation surfaces obtained from various pairs of images in the orbit 246. The surfaces are aligned with respect to t_n (ordinate) and the time interval $t_{n+k}-t_n$ (abscissa). The ranges of l and m, or the longitudinal and latitudinal sizes of the search region, for the fixed velocity ranges are narrower for shorter time interval; therefore, the peaks gets wider toward the left in Fig. 3.6a.

The heart of our method is to superpose the cross-correlation surfaces on the velocity coordinates. To do so, grid points have to be consolidated among different time intervals. We define the grid points based on the maximum time interval t_K-t_0 and introduce

$$u_{\hat{l},b} \equiv u_{\hat{l},b}^{0,K-1}, \tag{3.11}$$

$$v_{\hat{m}} \equiv v_{\hat{m}}^{0,K-1}, \tag{3.12}$$

where $\hat{l}$ and $\hat{m}$ are integers. The sets of $\hat{l}$ and $\hat{m}$ are the same as the sets of l and m for the maximum time interval. If the time interval is shorter, $r^{n,n+k}(\lambda_a,\phi_b,u_{l,b}^{n,n+k},v_m^{n,n+k})$ is linearly interpolated onto the $\hat{l}$-$\hat{m}$ grid as $r^{n,n+k}(\lambda_a,\phi_b,u_{\hat{l},b},v_{\hat{m}})$.

For brevity, we introduce a set of pairs used in the superposition and define $p=1,2,\cdots,P$ to represent the combinations of t_n and t_{n+k}. The spatially interpolated cross-correlations are then expressed as

$$r_p(\lambda_a,\phi_b,u_{\hat{l},b},v_{\hat{m}}) \equiv r^{n,n+k}(\lambda_a,\phi_b,u_{\hat{l},b},v_{\hat{m}}). \tag{3.13}$$

If the time interval $\delta t=t_{n+1}-t_n$ is constant irrespective of n, the number of combinations is

$$P = \frac{(n-s)(n-s-1)}{2}, \tag{3.14}$$

where $s\equiv\frac{\Delta t_{\min}}{\delta t}-1$.

The superposed cross-correlation surfaces is simply

$$r(\lambda_a,\phi_b,u_{\hat{l},b},v_{\hat{m}}) = \frac{1}{P}\sum_{p=1}^{P} r_p(\lambda_a,\phi_b,u_{\hat{l},b},v_{\hat{m}}). \tag{3.15}$$

Figure 3.6b shows it for the orbit 246. The false peaks are eliminated by the superposition. Therefore, cloud motion is uniquely identified.

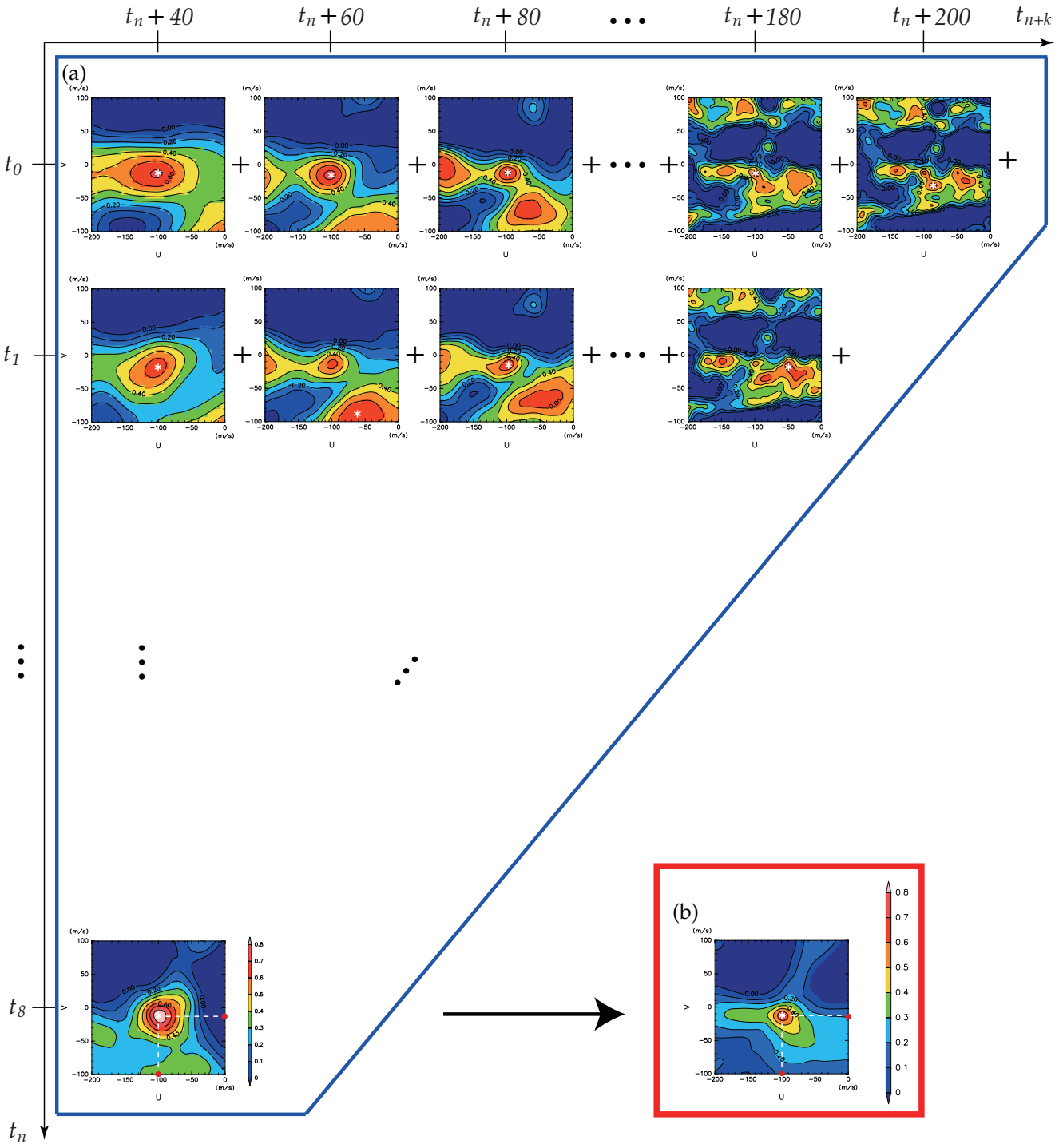

Figure 3.6: (a) Cross-correlation surfaces $r_p(\lambda_a, \phi_b, u_{l,b}, v_m)$ for individual image pairs, and (b) superposed cross-correlation $r(\lambda_a, \phi_b, u_{\hat{l},b}, v_{\hat{m}})$ defined by Eq. (3.15). Shown are the results for the orbit 246 and $(\lambda_a, \phi_b) = (96°\mathrm{E}, 24°\mathrm{S})$. In (a), the surfaces are aligned with respect to t_n (ordinate) and the time interval $t_{n+k} - t_n$ (abscissa). The $*$ mark designates the maximum. Here, $v_{\min}$ and $v_{\max}$ are set to -100 and 100 m s^{-1}, respectively, unlike the actual values (-70 and 70 m s^{-1}) used to estimate CMVs in this study.

The elimination of the false peaks is explained as follows. Suppose that we track a cloud feature around the position (x, y) at the initial time t_0, and that a similar feature exists around $(x + c, y + d)$ at the same time. The correlation between the two creates a false peak at the velocity $(u + c/\Delta t, v + d/\Delta t)$, where (u, v) is the actual velocity, and Δt is the time interval $t_{n+k} - t_n$. Thus, the peak appears at different positions (on the velocity coordinates) for different Δt. Therefore, the false peaks are decreased by superposition, while the true peak remains because $c = d = 0$. Note that the false peaks moves away as Δt is decreased, and $u + c/\Delta t \to \infty$ $(v + d/\Delta t \to \infty)$ when $\Delta t \to 0$ if $c \neq 0$ $(d \neq 0)$.

To further illustrate the effect of superposition, the superposed correlation surface is shown for different values of $\Delta t_{\min}$ in Fig. 3.7. Figure 3.7a is actually from a single pair, since $\Delta t_{\min} = 200$ min is equal to $t_{K-1} - t_0$. As $\Delta t_{\min}$ is reduced, the false peaks (F1, F2, $\cdots$) are lowered (Fig. 3.7a–d). Some false peaks are still comparable to the true peak at $\Delta t_{\min} = 80$ min (Fig. 3.7d). When $\Delta t_{\min}$ is further reduced to $\Delta t_{\min} = 40$ min (Fig. 3.6b), all of the false peaks are eliminated.

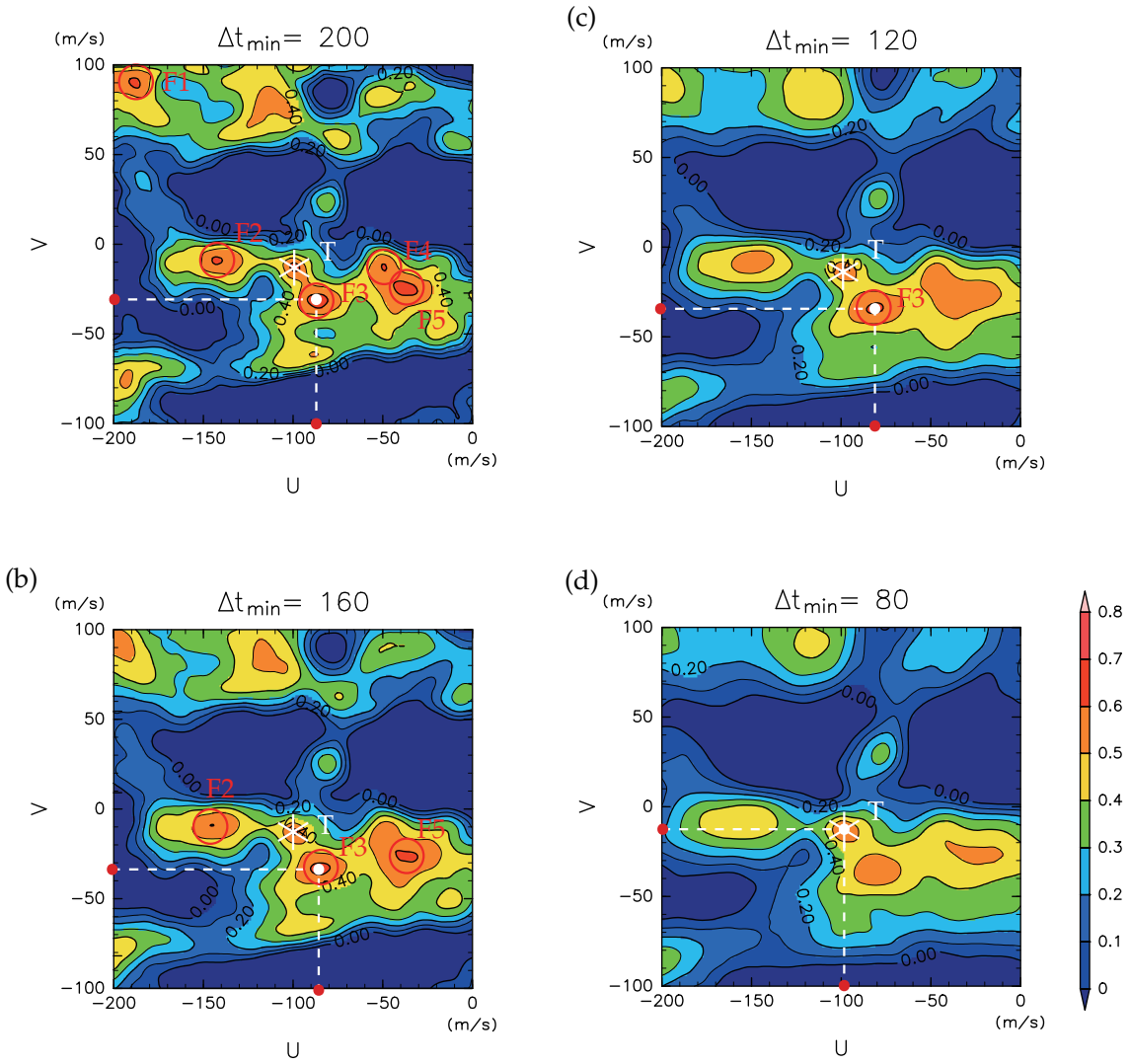

Figure 3.7: Superposed cross-correlation surfaces for various values of $\Delta t_{\min}$ for the same case as in Fig. 3.6: (a) 200 min, (b) 160 min, (c) 120 min, and (d) 80 min. The peak corresponding to the true velocity, which is evident in Fig. 3.6b, is designated by the $*$ mark and named "T", while the false peaks are named F1, F2, $\cdots$. The maximum correlation is denoted by the $\bullet$ mark. Here, $v_{\min}$ and $v_{\max}$ are set to -100 and 100 m s^{-1}, respectively, unlike the actual values (-70 and 70 m s^{-1}) used to estimate CMVs in this study.

The superposition also reduces the effect of noise, since the noise shift of correlation peaks are expected to be more or less random, so it is expected that superposition stabilize the peak positions. Noise can also create a false peak by creating a false pattern. If the noise is independent among brightness on the longitude-latitude coordinates, the effect is also weakened by the superposition.

3.4 Spatial moving average of cross-correlation surfaces (optional but used)

The method described in Section 3.2 uses a single template for each λ_a, ϕ_b, and t_n, as in the conventional cloud tracking, and superposition is made in the time domain over the combinations of t_n and t_{n+k} in order to increase accuracy and stability. It is also conceivable to make superposition in the space domain. Here, we introduce a spatial superposition as illustrated in Fig. 3.8. In this method, four additional template regions (a, b, d, and e) are introduced to the north, west, east, and south of the center region c, where they are overlapped by half. The superposition in the time domain is also used, so this method is actually to take a spatial moving average of the cross-correlation surfaces superposed in the time domain (Section 3.2) before deriving CMVs.

This process increases the number of target-template pairs, so it is expected to improve the estimation. On the other hand, it reduces the spatial resolution. Therefore, to use it or not should be determined practically in terms of the results and the spatial resolution required for the analysis desired. In what follows, the estimation based only on the superposition in time domain is referred to as ST (standing for the Superposition with Time) and the estimation based on the superposition both in the time and space domains as STS (standing for the Superposition with Time and Space).

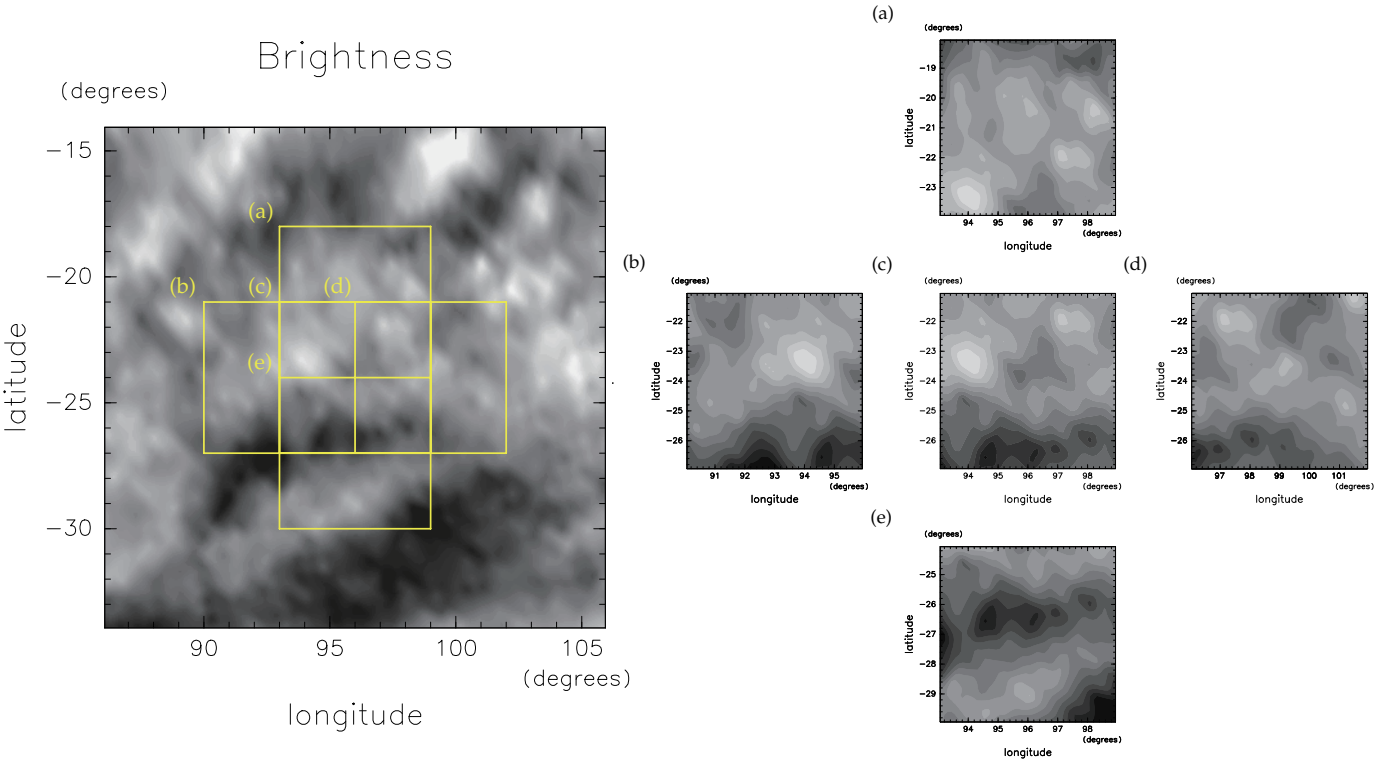

Figure 3.8: Left: configuration of the templates used for the STS estimation using spatial moving average (boxes a–e) overlayed on a preprocessed brightness F. Right: the distribution of F in the five template regions. The cloud tracking velocity is defined at the center of the box c.

3.5 Quality control

We evaluate the precision and error of the CMVs by the following three screenings:

1. Screening by $r_{\max}$ values: we reject CMVs where $r_{\max}(\lambda_a, \phi_b) < 0.6$.
2. Screening by statistical precision: as described in Section 4.1, the accuracy of cross-correlation peak is estimated statistically and is converted into a measure of the precision of CMVs, termed ε. A threshold for ε is applied to screen CMVs.
3. Screening by error: as described in Section 4.2, the error of CMVs, termed χ, is evaluated by comparing the results obtained from two subsets of images. A threshold for χ is applied to screen CMVs.

The screening 1 is always employed. The threshold, 0.6, is chosen to be slightly greater than 0.5 used by *Rossow et al.* (1990), since the lower bounds for $r_{\max}$ close to 0.5 are often so small that it is not suitable for the surface fitting in Section 4.1. The precision and error obtained by the screening 2 and 3 are used additionally to screen the results. The results obtained by the STS estimation screened by the screenings 1, 2, and 3 are referred to as STS123, and those screened only by the screening 1 and 2 are referred to as STS12. The same notation applies to the results of the ST estimation (ST12 and ST123). The threshold used for ε and χ are 20 m s^{-1} and 10 m s^{-1}, respectively.

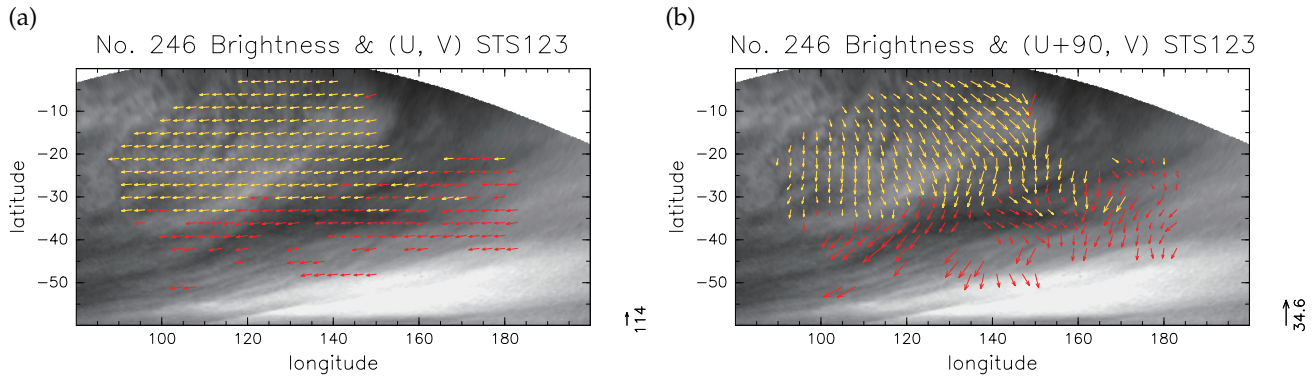

Figure 3.9: (a) The CMVs (arrows) obtained from the STS123 estimation for the orbit 246 overlayed on F at t_0. (b) as in (a) expect that a constant velocity of 90 m s^{-1} is added to the zonal component to highlight differences. Yellow arrows: CMVs with $\varepsilon < 10$ m s^{-1}; red arrows: CMVs with $10 \leq \varepsilon < 20$m s^{-1}.

3.6 Example of CMVs

Figure 3.9 shows the CMVs obtained from the orbit 246. As expected, they are predominantly westward (Fig. 3.9a). To emphasize their differences, a constant eastward velocity of 90 m s^{-1} is added in Fig. 3.9b. There is a bright region along the line between 80°E, 55°S and 170°E, EQ. The zonal velocity is relatively eastward and

westward to north and south of the bright band, respectively. Therefore, the flow over the band has a clockwise rotation. The velocity directions in other regions also have some correspondence with brightness features. However, this correspondence is not universal as shown in Section 5.

It should be stressed that, unlike in conventional cloud tracking, we did not apply any screening by comparing neighboring vectors. Subjective investigation for other orbits suggests that our full screening (123) works generally well but does not completely remove errors (see Section 5). To apply neighbor comparison would further improve the estimations.

Chapter 4

Precision and error evaluation

4.1 Statistical precision evaluation

At mid latitude, brightness patterns are elongated as can be seen in Fig. 3.1b. Movement of pure streaks can be identified only to their perpendicular directions, which disables two-dimensional tracking. If streaks are topped with small-scale features as in the regions β and γ in Fig. 3.2, tracking may be feasible. However, if patterns are dominated by streaks, tracking can be difficult. We propose an precision evaluation that explicitly treats this effect (the estimation 1 in what follows). We also use an precision evaluation suitable for isotropic cases (estimation 2).

We introduce a precision estimation based on the lower confidence bound of cross-correlation. Here, the sharpness of the highest peak of a cross-correlation surface is translated to the range of cloud motion velocity over which cross-correlation values are statistically indistinguishable. The estimation is formulated in what follows. Note that the confidence level used here is only in terms of the values of cross-correlation, and it does not provide a direct estimate of the confidence of CMVs. However, it is empirically useful as discussed and shown in Section 4.3.

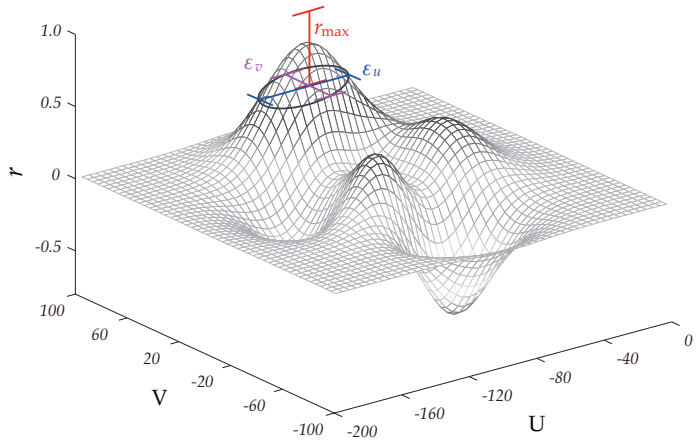

Figure 4.1: Schematic illustration of the CMV precision based on the lower confidence bound of the maximum cross-correlation coefficient $r_{\max}$. The curved surface represents the cross-correlation surface as a function of velocity. The oval is the cross section between the surface and the $r = r_{\mathrm{lb}}$ plane.

The 90%[1] confidence bounds of cross-correlation coefficient r is estimated as

$$Z - \frac{1.65}{\sqrt{M_e - 3}} \leq \eta \leq Z + \frac{1.65}{\sqrt{M_e - 3}}. \tag{4.1}$$

Here, $Z \equiv \tanh^{-1} r$, $\eta = \tanh^{-1} \rho$, where ρ is the population correlation coefficient, and M_e is the effective degree of freedom of the sample (*Fisher*, 1915). The cloud motion vector corresponds to the maximum cross-correlation coefficient $r_{\max}$ (see Fig. 4.1). From Eq. (4.1), its lower confidence bound is

$$r_{\mathrm{lb}} \equiv \tanh\left(Z_{\max} - \frac{1.65}{\sqrt{M_e - 3}}\right), \tag{4.2}$$

where $Z_{\max} \equiv \tanh^{-1} r_{\max}$. The effective degree of freedom M_{e} is calculated by using F in the template and target regions (Appendix A). Note that M_{e} is increased if P, the number of combinations, is increased from Eq. (A.5). Even though the number of pairs used in the STS estimation is five times as that in the ST estimation, the value of P is not changed when computing M_{e}. This treatment makes direct comparison of the precision estimation between the STS and ST results, but it results in an overestimation of the error of the STS results. Typical values of M_{e} in the orbit 246 are around 1,800 at low latitude (30°S–10°N) and around 900 at mid latitude (45°S–30°N). For reference, the upper and lower confidence bounds depending on r and M_{e} are shown in Fig. 4.2.

[1]The choice of the confidence level is ad hoc, since it is only the confidence level of cross-correlation, not CMV.

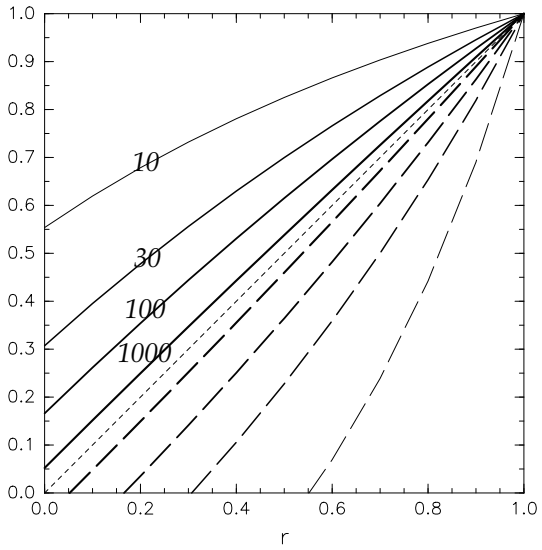

Figure 4.2: The 90% upper (solid lines) and lower (dashed lines) confidence bounds of cross-correlation coefficient r for some effective degrees of freedom (10, 30, 100, and 1000 as indicated in the figure). The dotted line is the diagonal line to indicate r itself.

We evaluate the precision of CMV by using the cross section between the cross-correlation surface and the $r = r_{\rm lb}$ plane (Fig. 4.1). The cross-correlation coefficient r is statistically indistinguishable from $r_{\rm max}$ if $r \geq r_{\rm lb}$. The accuracies of zonal and meridional velocities are defined as follows:

$$\varepsilon_u = \max(\varepsilon_{1u}, \varepsilon_{2u}), \tag{4.3}$$

$$\varepsilon_v = \max(\varepsilon_{1v}, \varepsilon_{2v}), \tag{4.4}$$

where ε_{1u}, ε_{1v}, ε_{2u}, and ε_{2v} are defined below. In other words, the precision is defined as the worse of the two estimates $\varepsilon_{1\xi}$ and $\varepsilon_{2\xi}$ ($\xi = u$ or v). The statistical precision for screening is evaluated as

$$\varepsilon = \max(\varepsilon_u, \varepsilon_v). \tag{4.5}$$

Note that ε is defined at each grid point $[a, b]$, so it is sometimes referred to as $\varepsilon(\lambda_a, \phi_b)$.

If the brightness pattern to track is dominated by (and is a part of) a streak, which is often the case at mid latitude, the cross-correlation peak is also elongated. In this case, the oval in Fig. 4.1 would look like the ellipse in Fig. 4.3a. The precision estimation 1 to derive $\varepsilon_{1\xi}$ is to cover such anisotropic cases, while the estimation 2 to derive $\varepsilon_{2\xi}$ is for relatively isotropic cases (Fig. 4.3b). In this study, we reject CMVs where $\varepsilon(\lambda_a, \phi_b) > 20$ m s^{-1} (screening 2 in Section 3.5).

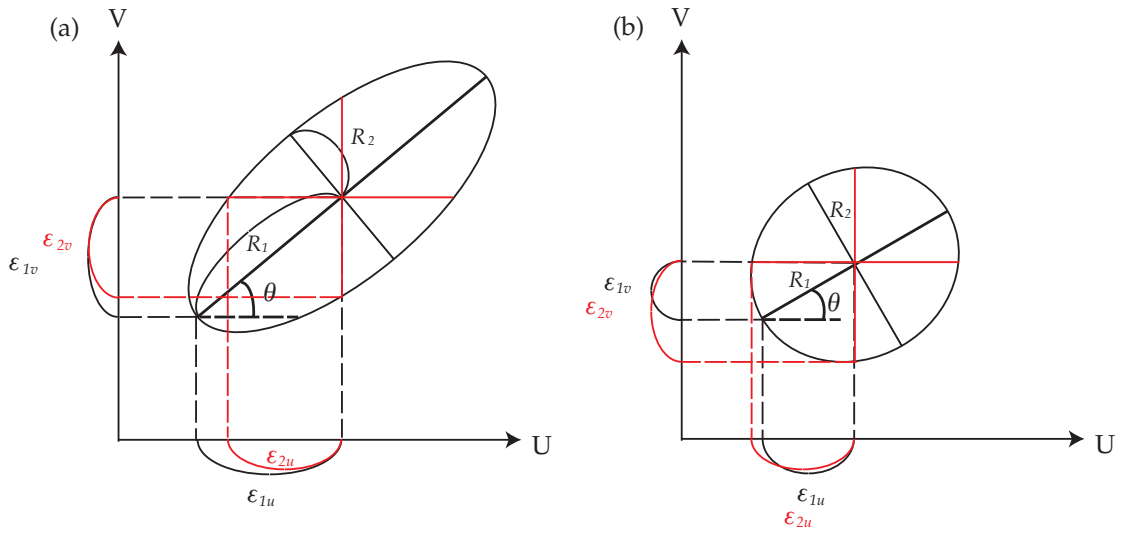

Figure 4.3: Schematic illustration of the precision estimations 1 and 2. (a) When the correlation surface above $r = r_{\rm lb}$ is elongated. (b) When it is relatively isotropic.

In the precision estimation 1, the correlation surface above $r_{\rm lb}$ is fitted by a elliptic paraboloid, as detailed in B.1. The precision is estimated as $\varepsilon_{1u} = R_1 \cos\theta$ and $\varepsilon_{1v} = R_1 \sin\theta$, where R_1 is the semi-major axis and θ is its angle in the u-v coordinate as shown in Fig. 4.3. If the fitting suggests that the peak is not an elliptic paraboloid, we set $\varepsilon_{1u} = \varepsilon_{1v} = \infty$, which results in the velocity rejected. Since the estimation 1 is to cover highly anisotropic cases, it is meaningless when the number of grid points used is too few. We calculate it only when the number is greater than 20, even though the minimum number required for the fitting is 6. When $\varepsilon_{1\xi}$ is not calculated, we rely only on the estimation 2.

In the precision estimation 2, quadratic functions are fitted to the cross sections of correlation surface along the u and v axes. The precision is estimated as $\varepsilon_{2u} = \sqrt{\frac{(r_{\rm max} - r_{\rm lb})}{-c_0}}$ and $\varepsilon_{2v} = \sqrt{\frac{(r_{\rm max} - r_{\rm lb})}{-c_1}}$, where c_0 and c_1 are fitting coefficients (B.2). When the number of grid points where $r \geq r_{\rm lb}$ is smaller than three, the fitting is not available. In this case, $r_{\rm max}$ is significant, so ε_{2u} and ε_{2v} are set to the grid-point intervals:

$$(\varepsilon_{2u}, \varepsilon_{2v}) = \left(\frac{\Delta\lambda R_c \cos\phi}{t_{K-1} - t_0}, \frac{\Delta\phi R_c}{t_{K-1} - t_0} \right). \tag{4.6}$$

4.2 Error evaluation by comparing CMVs

If many brightness images are available during an orbit, as is the case for the orbit 246, one can estimate the error by subdividing them into two groups, making cloud tracking for each group, and comparing the results. Here, we refer the entire images used from an orbit as the group A, and we define the groups B and C as consisting of odd- and even-numbered images, respectively (Fig. 4.4). We refer to the CMVs obtained from group X (X=A, B, C) as the estimate X and use X as suffix. As for the orbit 246, the number of the pairs used in the estimates

A, B, and C are 45, 15, and 10, respectively (Fig. 4.4). Note that the estimate A is the full estimate described in Section 3.6, and the estimates B and C are independent of each other.

We write the true velocity, which cannot be measured, at $\lambda = \lambda_a$ and $\phi = \phi_b$ as $[u_t(\lambda_a, \phi_b), v_t(\lambda_a, \phi_b)]$ and introduce the absolute values of vector differences as

$$\sigma_X(\lambda_a, \phi_b) \equiv \sqrt{\{u_t(\lambda_a, \phi_b) - u_X(\lambda_a, \phi_b)\}^2 + \{v_t(\lambda_a, \phi_b) - v_X(\lambda_a, \phi_b)\}^2} \quad \text{for } X = \mathrm{A}, \mathrm{B}, \mathrm{C}, \tag{4.7}$$

and

$$\sigma_{\mathrm{BC}}(\lambda_a, \phi_b) \equiv \sqrt{\{u_{\mathrm{B}}(\lambda_a, \phi_b) - u_{\mathrm{C}}(\lambda_a, \phi_b)\}^2 + \{v_{\mathrm{B}}(\lambda_a, \phi_b) - v_{\mathrm{C}}(\lambda_a, \phi_b)\}^2}. \tag{4.8}$$

If we assume that CMVs derived from a single pair has error with a normal distribution and the error is independent among pairs, we can expect the following relations:

$$\langle \sigma_{\mathrm{B}}^2 \rangle = \frac{P}{P_{\mathrm{B}}} \langle \sigma_{\mathrm{A}}^2 \rangle, \tag{4.9}$$

$$\langle \sigma_{\mathrm{C}}^2 \rangle = \frac{P}{P_{\mathrm{C}}} \langle \sigma_{\mathrm{A}}^2 \rangle, \tag{4.10}$$

$$\langle \sigma_{\mathrm{BC}}^2 \rangle = \langle \sigma_{\mathrm{B}}^2 \rangle + \langle \sigma_{\mathrm{C}}^2 \rangle, \tag{4.11}$$

and thus

$$\langle \sigma_{\mathrm{A}}^2 \rangle = \left(\frac{P}{P_{\mathrm{B}}} + \frac{P}{P_{\mathrm{C}}} \right)^{-1} \langle \sigma_{\mathrm{BC}}^2 \rangle, \tag{4.12}$$

where P, P_{B}, and P_{C} are the numbers of the pairs in the groups A, B, and C, respectively, and angle brackets express expected values. As for the orbit 246, $\sqrt{\frac{P}{P_{\mathrm{B}}}} = 1.7$, $\sqrt{\frac{P}{P_{\mathrm{C}}}} = 2.1$, so the expected error of the estimates B and C are approximately twice as the estimate A from Eqs. (4.9) and (4.10).

The half-value width at the 95% confidence level for the estimate A is $1.96\sqrt{\langle \sigma_{\mathrm{A}}^2 \rangle}$. Therefore, we can introduce a measure of error as

$$\chi(\lambda_a, \phi_b) \equiv 1.96 \left(\frac{P}{P_{\mathrm{B}}} + \frac{P}{P_{\mathrm{C}}} \right)^{-\frac{1}{2}} \sigma_{\mathrm{BC}}(\lambda_a, \phi_b). \tag{4.13}$$

Note that χ is defined at each grid point (λ_a, ϕ_b). Therefore, we can apply it to screen CMVs. In this study, we reject CMVs where $\chi(\lambda_a, \phi_b) > 10$ m s^{-1} (the screening 3 in Section 3.5).

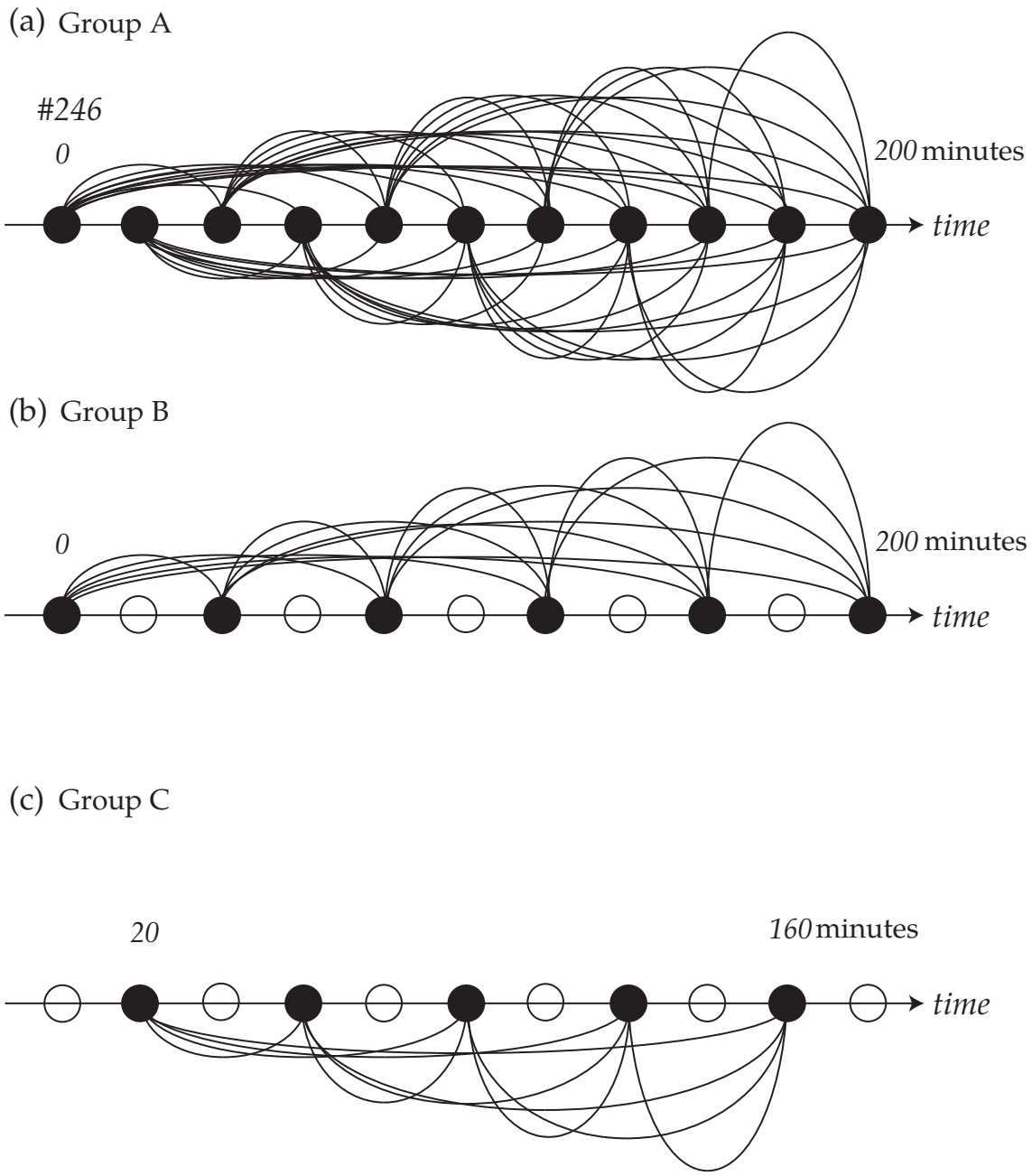

Figure 4.4: Illustration of the observation times (circles) and the pairs to compute cross-correlation (curves) for the group (a) A, (b) B, and (c) C. The number of times, 11, is based on the orbit 246, in which observation is made every 20 min.

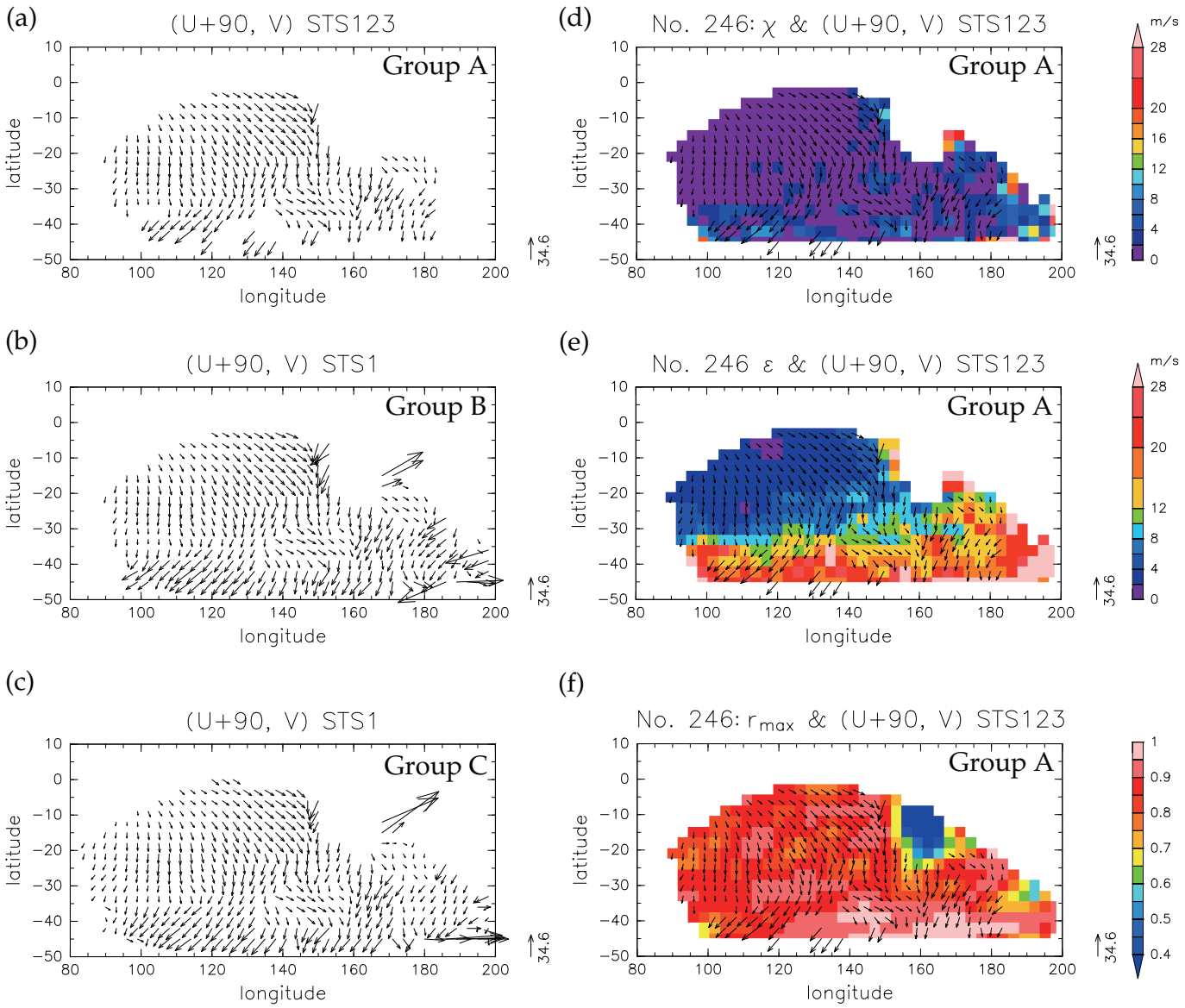

Figure 4.5: CMVs from the orbit 246. (a) Full STS123 result derived from the group A. Zonal winds are offset by 90 m s^{-1} (shown are $[u + 90$ m $s^{-1}, v]$). (b) CMVs from the group B screened only by the $r_{\max}$ values (screening 1). (c) As in (b) but for the group C. (d) Color shading: χ (shown only where $r_{\max} \geq 0.6$); vectors: as in (a). (e) As in (d) but the color shading is for ε. (f) color shading: $r_{\max}$ (no screening); vectors: as in (a).

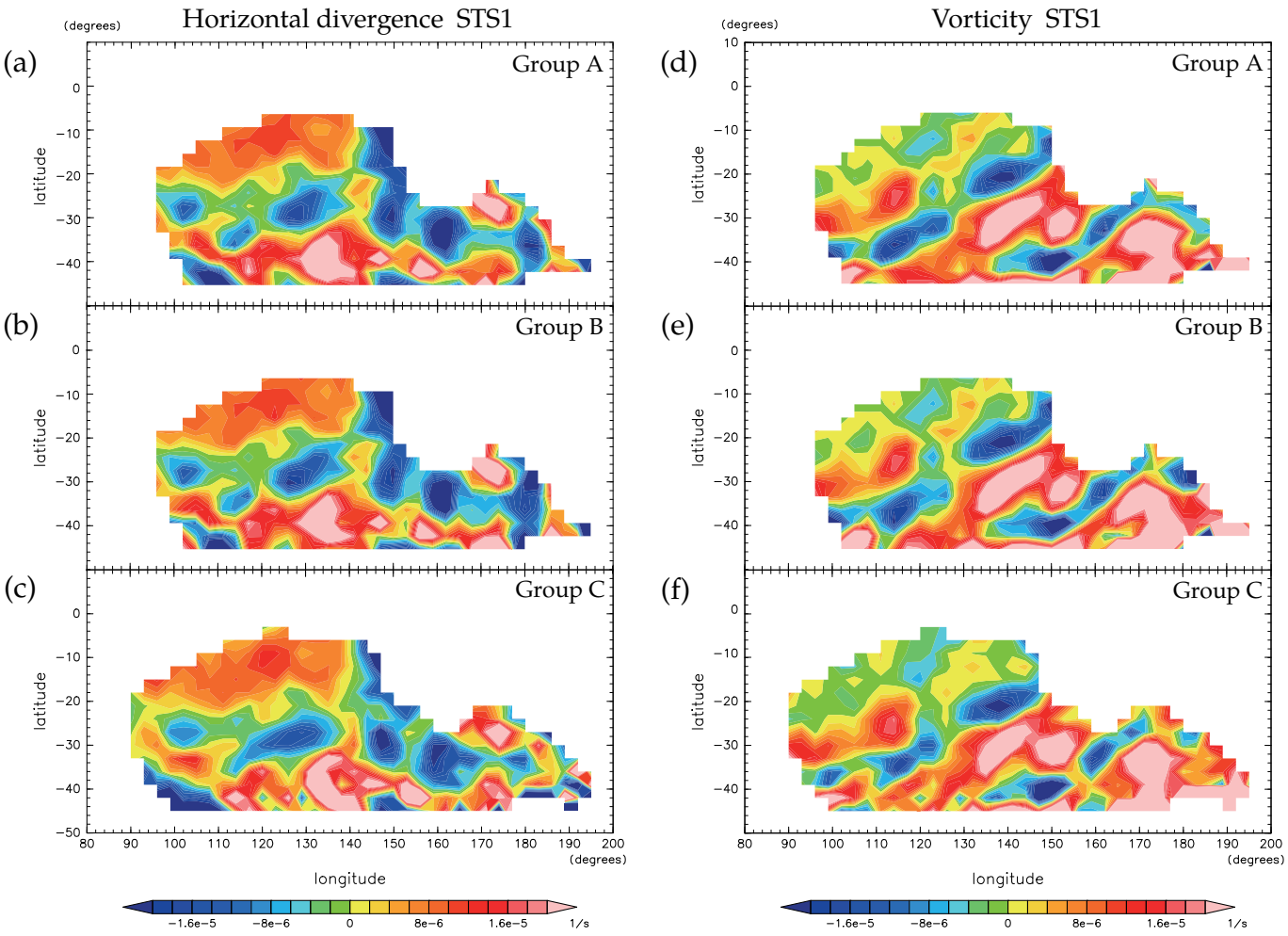

Figure 4.6: As in Fig. 4.5a–c but for horizontal divergence (a–c) and vorticity (d–f) obtained from CMVs screened by the screening 1.

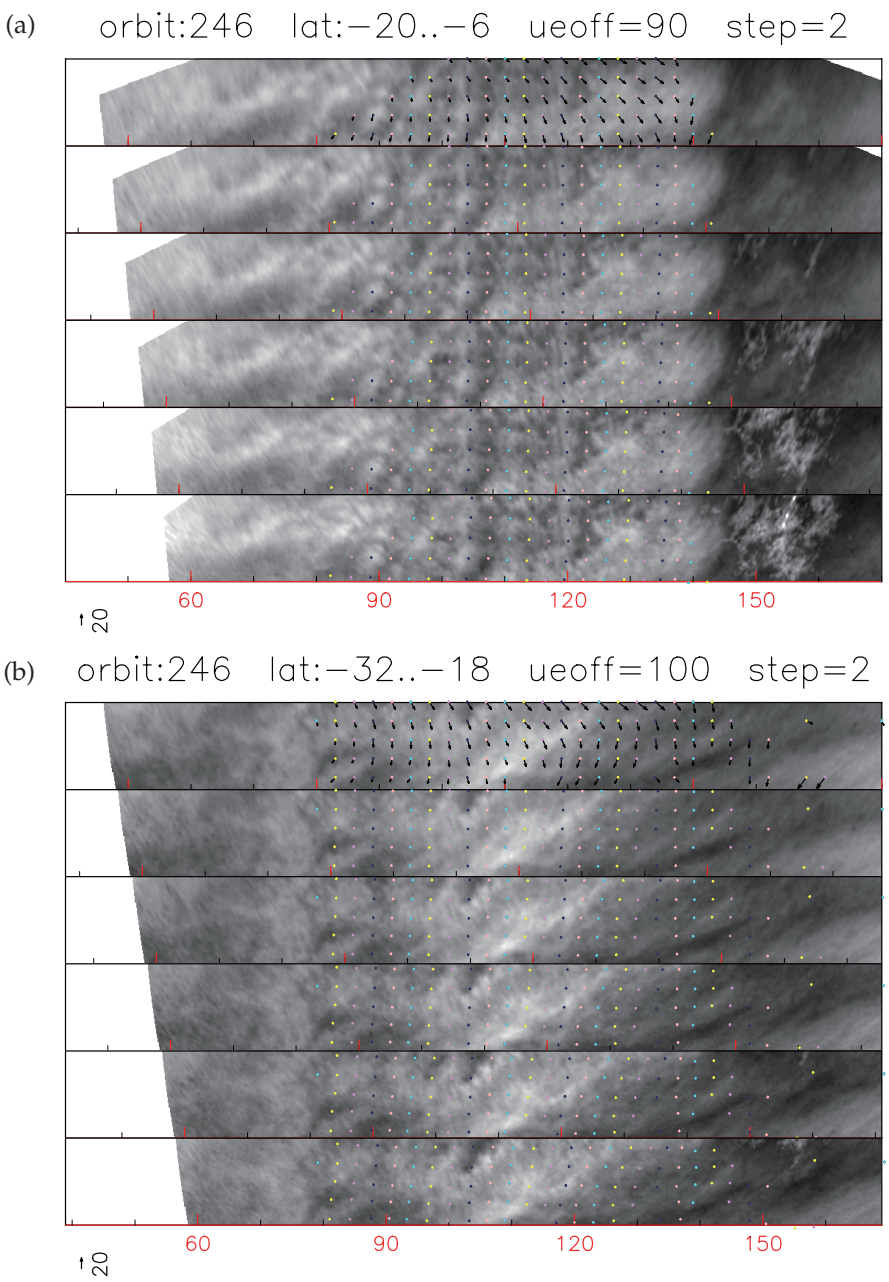

Figure 4.7: CMVs that satisfy $\varepsilon < 10$ m s $^{-1}$ and $\chi < 10$ m s^{-1} (arrows), trajectories corresponding to the CMVs (colored dots), and the preprocessed brightness F (shading) for the orbit 246. The latitudinal ranges covered are (a) 20°S–6°S and (b) 32°S–18°S. Zonal winds corresponding to the solid body rotations that have zonal velocities (a) -90 m s^{-1} and (b) -100 m s^{-1} at the equator are subtracted from the CMV arrows (unlike in Fig. 3.9 where a uniform zonal wind is subtracted). To show their scales, an arrow whose length corresponds to 20 m s^{-1} is shown near the lower-left corner of each panel. The brightness is shown for every 40 min (thus shown are six of the eleven images used to derive the CMVs). To ease visual tracking, images are shifted longitudinally with time (see the red tick marks), which corresponds to the longitudinal shift by the solid body rotations subtracted from CMV arrows. The dots are advected by CMVs constantly with time. Caution: there are small-scale features associated with instrumental error in (a) around the longitude 150° at later times; they do not move in the original images.

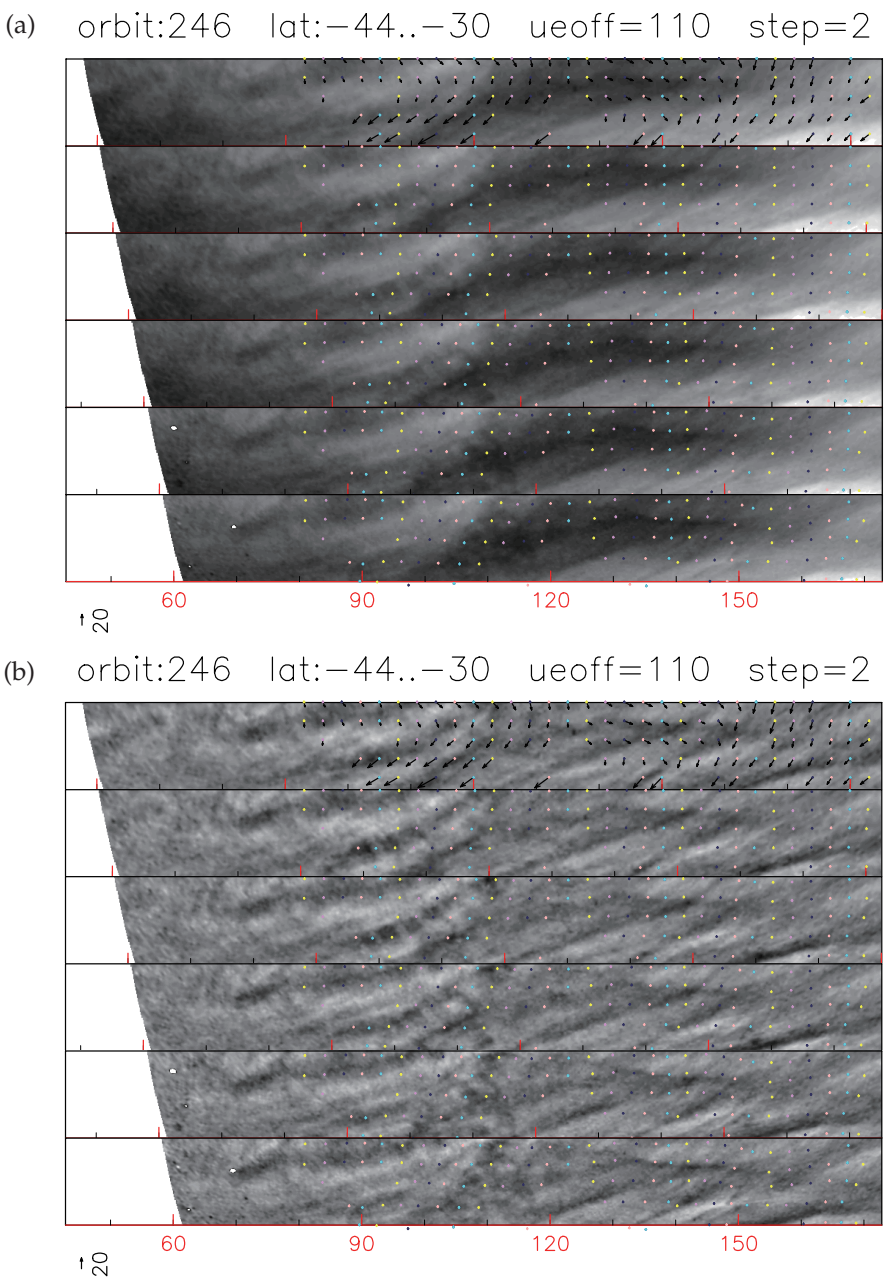

Figure 4.8: (a) As in Fig. 4.7 but for the latitudinal range 44°S–32°S. The threshold of ε to show CMVs and trajectories are loosened to 20 m s^{-1}. (b) As in (a) but the brightness is filtered by a high-pass filter to pass features having scales smaller than $6^{\circ} \times 6^{\circ}$ (by using a Tukey cosine filter whose full width at half maximum is 6°).

4.3 Results

Figure 4.5 shows the velocity estimates A, B, and C for the orbit 246. They are remarkably similar, even though the pairs used in the estimates B and C are much fewer than those in the estimate A. The error measure χ, which is obtained from the difference between B and C, is smaller than 2 m s^{-1} at many grid points (Fig. 4.5d). The precision ε, which represents the sharpness of the cross-correlation surface peaks, is generally greater than χ (Fig. 4.5e). Figs.

4.5d and e indicates that CMVs are screened more by ε than χ. It increases with latitude, since brightness features are obscure and often elongated at mid latitude. The maximum cross-correlation $r_{\max}$ is generally high irrespective of latitude (Fig. 4.5f). The low $r_{\max}$ values around 160°E, 10°S are due to the dominance of noise. We further compare horizontal divergence and vorticity in Fig. 4.6. Note that they are computed from CMVs screened only by $r_{\max}$ (STS1). Even though the derivative operations to compute them enhance small-scale features, patterns seen in the figure are remarkably similar among the estimates. The result gives us some confidence on the CMVs down to $\mathcal{O}(1000)$ km. However, the small-scale features may still not be reliable especially at mid latitude where ε is large (note that the scale of error in the derivative of velocity, $\Delta U/L$, is 1×10^{-5} s^{-1} if the error scale of velocity ΔU is equal to 10 m s^{-1} and the length scale L is equal to 1000 km).

Figure 4.7 shows how well our CMVs represent the evolution of brightness features for the orbit 246. Shading expresses the preprocessed brightness F at every 40 min (corresponding to images used in the group B introduced in Section 4.2), and colored dots represent trajectories advected by CMVs having ε values smaller than 10 m s^{-1}. Initial positions of the trajectories are at the three-degree grid points. In order to highlight spatial features, zonal winds corresponding to a solid body rotation (-90 or -100 m s^{-1} at the equator) is subtracted from CMVs (arrows), and the longitudinal axes are shifted accordingly with time.

In this figure, it is easily seen that most trajectories follow small-scale features, even though a CMV represents a large area; the template size is $6° \times 6°$, and the STS spatial moving average is applied (Section 3.4). This result suggests the overall validity of our cloud tracking. If a CMV has an error of 10 m s^{-1}, for example, its trajectory is deviated by 1.1° (if in the meridional direction) over the 200-min period. We examined the trajectories visually, and it appeared that many of them have accuracy better than 1°, which is roughly consistent with the ε values. However, we cannot visually distinguish a difference corresponding to 2 m s^{-1}, a typical value of χ at low latitude.

Figure 4.8a is similar to Fig. 4.7 but for mid latitude. Since small-scale features are not clear there, high-passed brightness is shown in Fig. 4.8b (here, the high-pass filter is devised to mimic the subtraction of means when cross-correlations are computed). In Fig. 4.8, the threshold ε value is set to 20 m s^{-1}; note that most of CMVs here have ε greater than 10 m s^{-1} (Fig. 4.5e). Small-scale features are dominated by elongated slantwise patterns, and to visually identify cloud motions is more difficult than in Fig. 4.7, which is consistent with the large ε values at mid latitude.

We have done similar visual inspection for many orbits, and we found that ε values are more consistent with our subjective impression than χ values. This is probably because ε values indicate the ranges over which cross-correlations are indistinguishable. Also, ε reflects the size of the features to track. Therefore, ε can be regarded as a measure of the precision of visual (manual) cloud tracking. Values of χ are generally much smaller than ε, as shown below. Naïve visual inspection described above treats each image independently, so it is not benefitted by the superposition using many images. Therefore, the smallness of χ may suggest that our method can improve CMVs beyond the limit of manual tracking, but we cannot verify it with visual inspection.

We now examine the error for multiple orbits. Figure 4.9 shows the rms and median of χ where LTAN is between 9 am and 15 pm in the period 2. The results are shown for ten orbits from 243 to 267. In the other orbits, the number of images having acceptable quality and resolution (see Section 2) is fewer than 4, which is the minimum number to compute χ. The error is generally smaller at low latitude than at mid latitude. The median values are generally smaller than the rms values, since the latter are more sensitive to outliers, which are positive-only. For the same reason, the median values are less sensitive to screening than the rms values. The rms values are decreased from STS1 (in which only the screening 1 is applied) to STS123 (in which the screening 1, 2, and 3 are applied) because the screening removes outliers. Table 4.1 summarizes the rms and median of χ averaged over the ten orbits. It is noteworthy that the rms χ value is as small as 1.4 m s^{-1} (1.8 m s^{-1}) at low (mid) latitude. Table 4.1 also shows the measures of error in horizontal divergence χ_δ and vorticity χ_ζ; these quantities are defined as in Eq. (4.13) but for using horizontal divergence for χ_δ and vorticity for χ_ζ to compute σ_B and σ_C. The median values are smaller than the typical strength of divergence and vorticity, but rms values are not.

The rms and median values of ε are summarized in Table 4.2. As mentioned earlier for the orbit 246, these values are greater than those of χ. The rms and median values of ε are close, suggesting that large ε values are not outliers. At mid latitude, the rms and median values are close to the imposed threshold of 20 m s^{-1}. It suggests that the screening by ε is prevalent at mid latitude, as can be seen in Fig. 4.5 for the orbit 246.

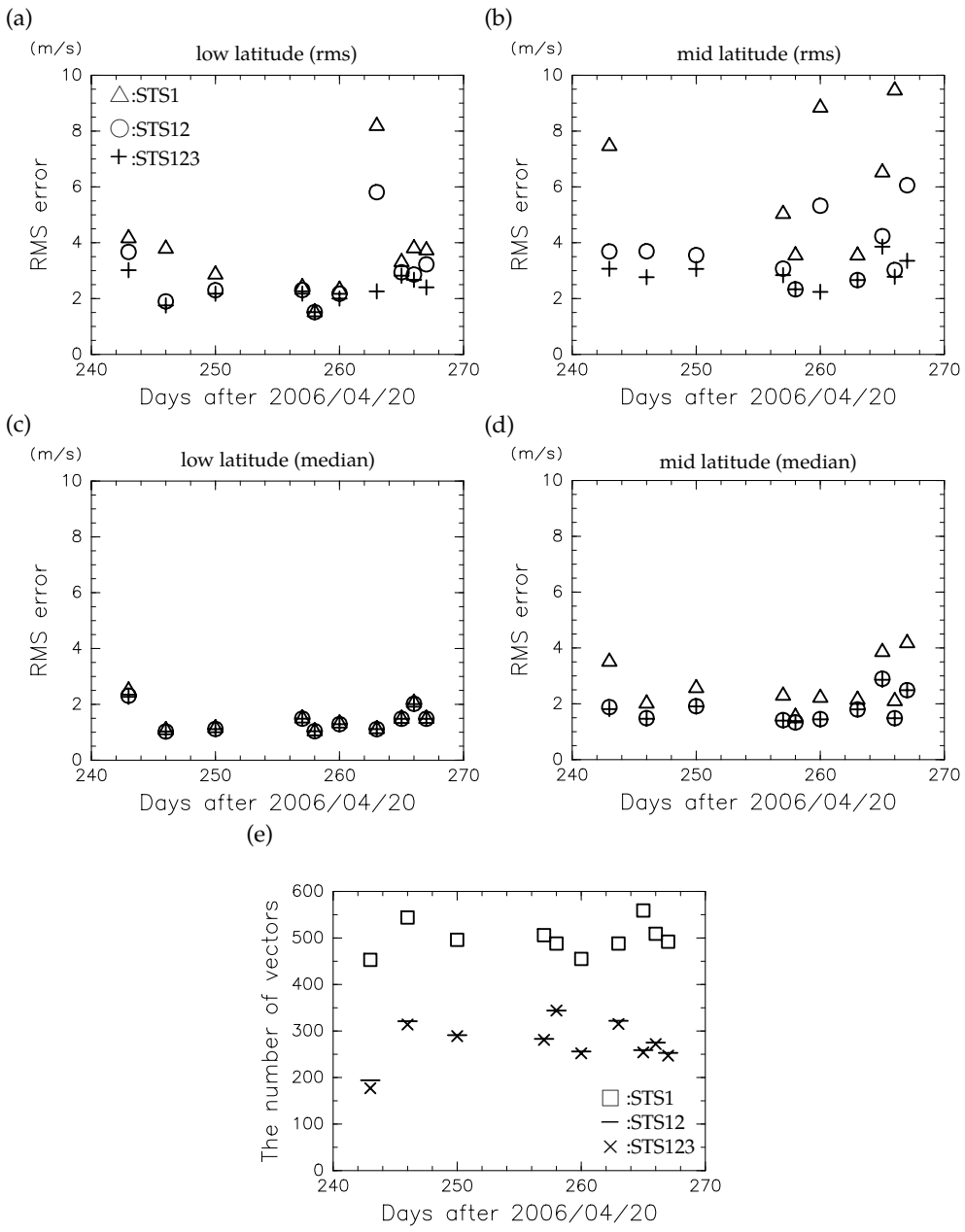

Figure 4.9: The rms (a, b) and median (c, d) of χ, and the number of vectors (e) obtained from the ten orbit from 243 to 267 by using the STS1, STS12, and STS123 estimations. (a, c) Averaged over 30°S–10°N; (b, d) averaged over 45°S–30°S.

As mentioned in Section 3.4, the STS (superposition in time and space) estimation, which we primarily rely on in this study, is expected to have smaller errors than the ST (superposition in time) estimation. The errors are compared in Fig. 4.10 and Table 4.1, in which the expectation is verified.

STS123

	low latitude (10°N–30°S)		mid latitude (30°S–45°S)	
	rms value	median value	rms value	median value
wind velocity (χ)	2.3 m s^{-1}	1.4 m s^{-1}	2.9 m s^{-1}	1.8 m s^{-1}
horizontal divergence (χ_δ)	6.8×10^{-6} s^{-1}	2.4×10^{-6} s^{-1}	1.9×10^{-5} s^{-1}	5.9×10^{-6} s^{-1}
vorticity (χ_ζ)	6.5×10^{-6} s^{-1}	2.7×10^{-6} s^{-1}	1.6×10^{-5} s^{-1}	5.9×10^{-6} s^{-1}

ST123

	low latitude (10°N–30°S)		mid latitude (30°S–45°S)	
	rms value	median value	rms value	median value
wind velocity (χ)	3.1 m s^{-1}	2.0 m s^{-1}	3.7 m s^{-1}	2.5 m s^{-1}
horizontal divergence (χ_δ)	2.1×10^{-5} s^{-1}	5.7×10^{-6} s^{-1}	4.0×10^{-5} s^{-1}	1.3×10^{-5} s^{-1}
vorticity (χ_ζ)	1.8×10^{-5} s^{-1}	5.0×10^{-6} s^{-1}	3.2×10^{-5} s^{-1}	1.1×10^{-5} s^{-1}

Table 4.1: The rms and median of χ from CMVs, horizontal divergence (χ_δ), and vorticity (χ_ζ) averaged horizontally and over the ten orbits from 243 to 267. The horizontal averaging is made separately between 30°S and 10°N ("low latitude") and between 45°S and 30°S ("mid latitude"). The upper and lower tables show the STS123 an ST123 results, respectively.

precision evaluation	low latitude		mid latitude	
	rms value	median value	rms value	median value
statistical precision	9.1 m s^{-1}	7.6 m s^{-1}	14.1 m s^{-1}	13.8 m s^{-1}

Table 4.2: The rms and median of ε averaged horizontally and over the ten orbits from 243 to 267. Shown separately for low and mid latitudes as in Table 4.1.

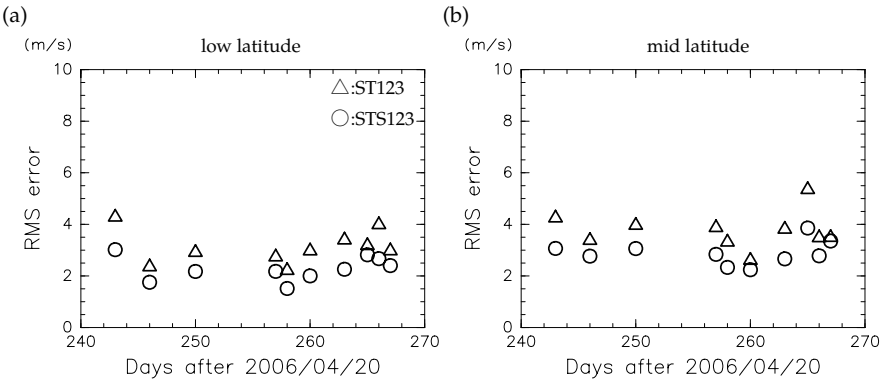

Figure 4.10: The rms of χ obtained from the ST123 (triangles) and STS123 (circles) results averaged over (a) 30°S–10°N and (b) 45°S–30°S.

In this study, we apply the optical correction and the limb fitting proposed by *Kouyama et al.* (2013b) and *Ogohara et al.* (2012) as described in Section 3.1. To examine their effect, we compare the CMVs with and without the correction (Fig. 4.11). The error is generally increased if the correction is not applied. For some cases, the error is increased two to three times. Furthermore, the number of CMVs that passed the screening is decreased slightly. Recently, *Limaye et al.* (2015) proposed a different interpretation for the necessity of image correction and an alternative correction for VMC, but Fig. 4.11 suggest that the present correction is useful.

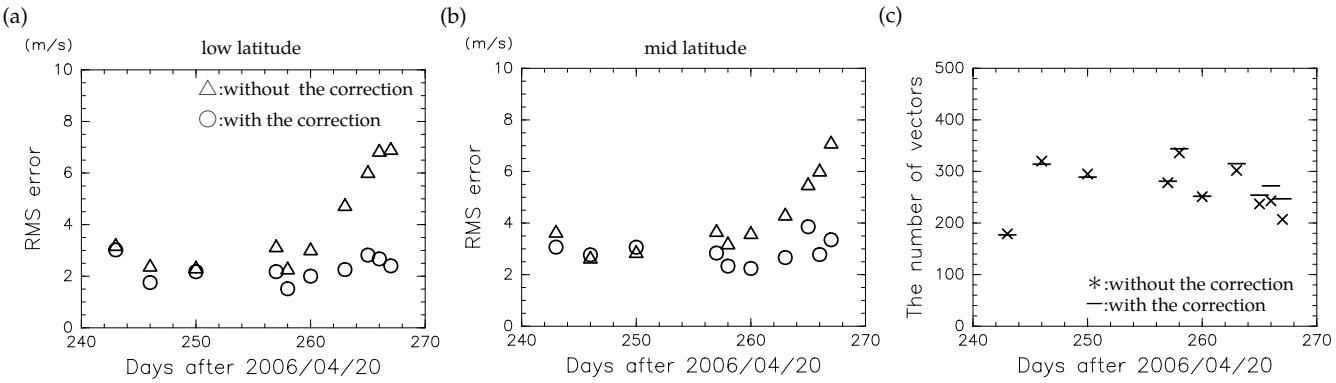

Figure 4.11: The rms (a–b) of χ and the number of vectors (c) obtained from the STS123 estimation with ("$\circ$" or "$-$") and without ("$\triangle$" or "$*$") the optical and pointing-angle corrections. Averaged over (a) 30°S–10°N, (b) 45°S–30°S.

Figure 4.12 shows the median of χ, the number of obtained CMVs as a function of latitude, and the number of images used to derive CMVs for orbits in the periods 2 and 3. The number of CMVs is generally small when LTAN is close to the evening, as expected. The median of χ in the period 2 is generally smaller than that in the period 3, while the number of the CMVs are generally greater in the period 2. This result is consistent with the fact that the number of images used to derive CMVs is generally greater in the period 2. However, the median χ and the number of CMVs are not simple functions of the number of images. By inspecting data for each orbit by eyes, it is observed that data quality is not uniform during the periods, and it affects the overall quality of the CMV estimation.

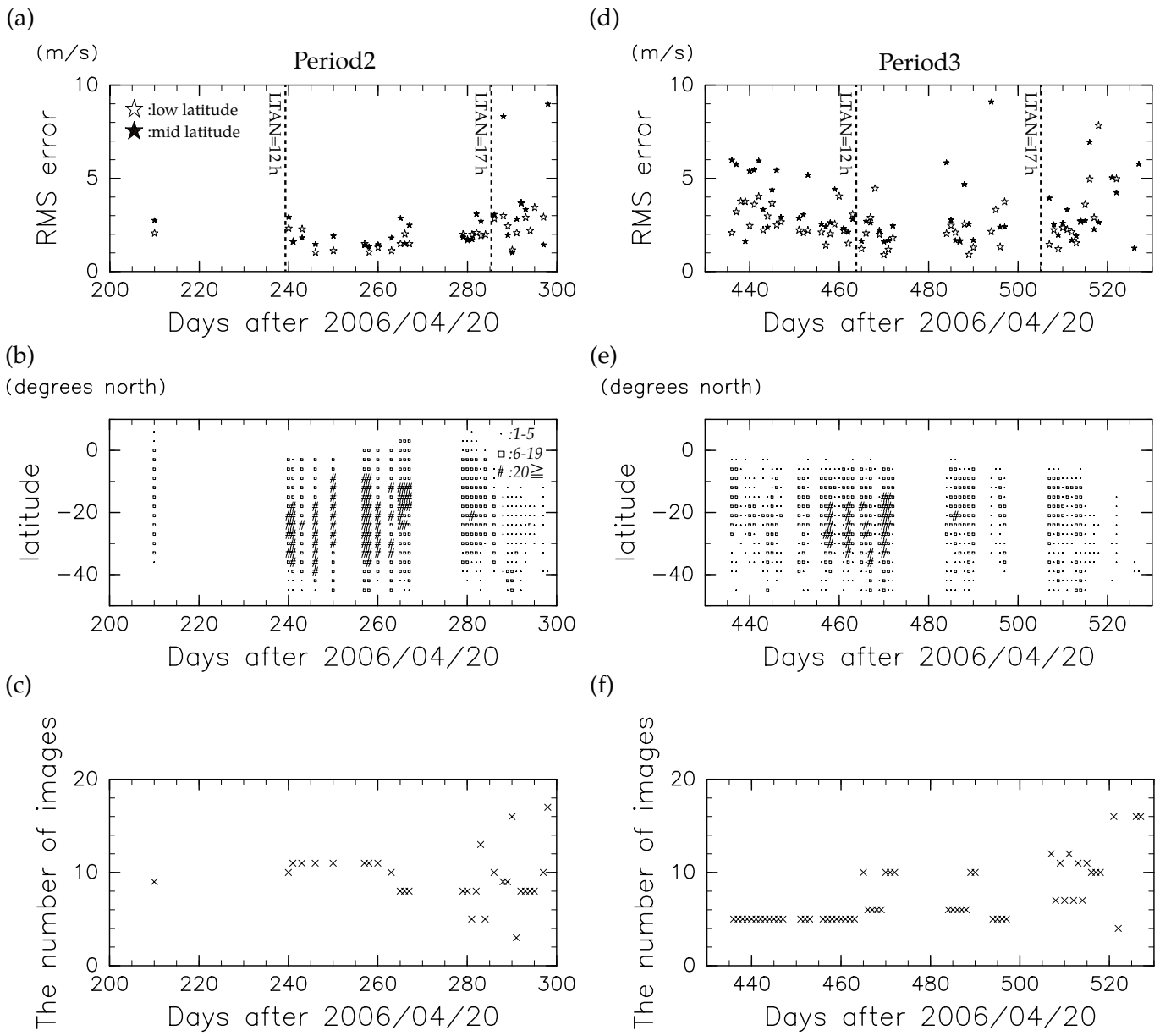

Figure 4.12: (a) The median of χ (from the STS123 results) averaged over 30°S–10°N (outlined $\star$ marks) and 45°–30°S (filled $\star$ marks), (b) the number of CMVs for each latitude (dots for 1–5, squares for 6–19, and sharps if greater or equal to 20), and (c) the number of images used, for the period 2. (d)–(f) as in (a)–(c) but for the period 3. Dotted (dashed) lines in (a) and (d) show when LTAN is 12 (17) h.

4.4 Sensitivity to the template size or to the scale of tracked features

Kouyama et al. (2013a) investigated the sensitivity of CMVs (obtained from two images) to the size of template regions by changing it from $2° \times 2°$ to $10° \times 10°$. They showed that mean winds are not statistically different across the template sizes, but the results exhibit a large variance around the smallest size. They then recommended the template size of $6° \times 6°$ and used it for their analysis. Here we describe the sensitivity of our CMVs to the template

size. We then briefly examine the effect of high-pass filtering of brightness prior to cloud tracking, which we did not use elsewhere in this study.

We conducted the STS estimation by changing the template size from 6°×6° to 4°×4° and compared the results for the orbits 246–267 by interpolating the former onto the latter's grid points. The mean value of the vector difference (the length of the difference of the two estimates of a cloud motion vector) at each grid point is 2.1 m s^{-1} at low latitude (30°S–10°N) and 2.7 m s^{-1} at mid latitude (45°S–30°S). These values are small, but they are slightly greater than the mean χ values, suggesting that χ does not cover the entire ambiguity of cloud motion.

The ratio of the grid points at which the difference is smaller than 2 m s^{-1} is 60 % (48 %) at low (mid) latitude, and the ratio of the grid points where the difference is greater than 4 m s^{-1} (10 m s^{-1}) is 10 % (0.2 %) at low latitude and 18 % (0.7 %) at mid latitude. Therefore, at most grid points, the difference is too small to distinguish by manual tracking (see Figs. 4.7 and 4.8, and the text discussing them). Where the difference of the two estimates is relatively large, the reliability of CMV may be relatively low. As one can thus expect, the difference is positively correlated with χ (and also with ε) significantly, but the correlations are quite weak (around 0.1).

The calculation of cross correlation includes the subtraction of mean values. Therefore, to use a smaller template size is equivalent to track smaller-scale features. We additionally conducted a CMV computation in which the template size is set to 6°×6° but a high-pass filter (to roughly pass features smaller than 3°) is applied in the preprocess. We examined the differences visually using figures for each orbit (not shown), and we found that the differences between without and with the filter is similar to the differences between 6°×6° and 4°×4° templates, respectively, as described above. Therefore, these differences are consistently explained in terms of the sensitivity of CMVs to the sizes of features to track.

From these results, we speculate that the temporal change of cloud features causes ambiguity in the determination of cloud motions, thereby causing the scale dependence. Note that the temporal change can be due to actual brightness change over a few hours as well as due to the change of the satellite position, which affects resolution and satellite zenith angle. If the changes are gradual with time, the ambiguity is not covered by χ. Therefore, we guess that the accuracy of CMVs may not be as good as χ values suggest, but it is not drastically worse than it, since the CMV differences associated with different template (or feature) sizes are not large.

Chapter 5

Features of CMVs and comparison with previous studies

In this section, we investigate the STS123 results of CMVs. Figure 5.1 shows the CMVs for the ten orbits examined in Section 4.3. Except for the orbit 243, the number of CMVs that passed the screening are similar to that for the orbit 246 shown in Section 3.6. Also, the $r_{\max}$, ε, and χ values are similar to the results from the orbit 246 (figure not shown). Namely, ε increases with latitude (it jumps up at around 30°S), while $r_{\max}$ is high irrespective of latitude, and χ is generally smaller and is less dependent on latitude than ε. Even though CMVs have been screened, some of them do not appear realistic, as is especially evident for the solitary ones such as the CMV at 204°E, 21°S for the orbit 263. In many orbits, some of the CMVs at mid latitude are deviated eastward anomalously in comparison with surrounding CMVs. This is especially the case near the eastern edge of observations where the spacecraft zenith angle is large. We visually examined the validity of the eastward deviation in 130°E–150°E, 39°S–42°S and 165°E–180°E, 27°S–36°S by trying to manually track features, and we found that it is difficult because F values there are quite featureless. On the other hand, we could manually trace features around the regions where CMVs are less deviated.

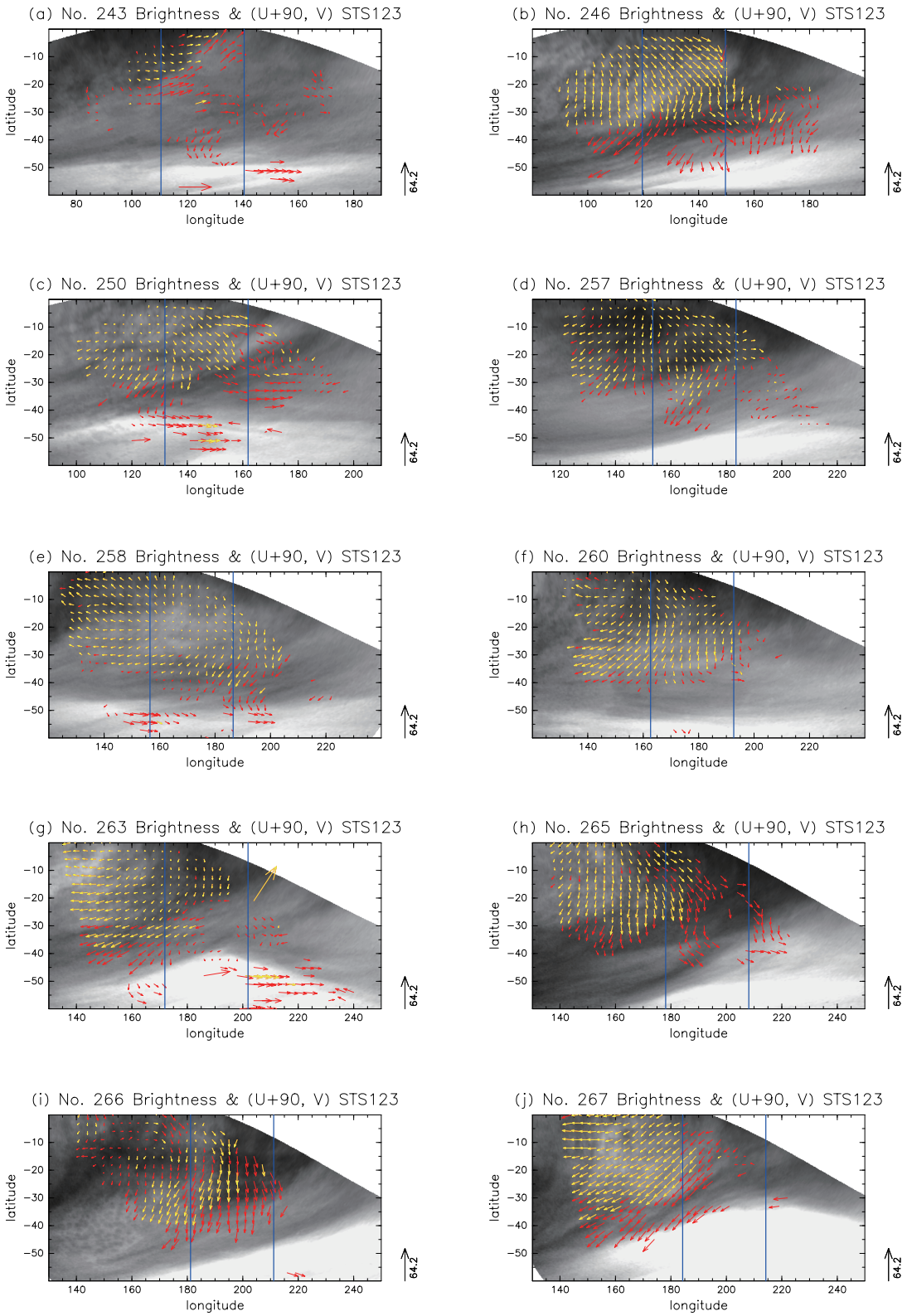

Figure 5.1: CMVs offset by [90, 0] m s^{-1} as in Fig. 4.5a (arrows) and F at t_0 (color shading) obtained from the ten orbits from 243 to 267 as in Fig. 4.9. The right and left red lines indicate local times 11 am and 13 pm, respectively. Yellow arrows: CMVs with $\varepsilon < 10$ m s^{-1}; red arrows: CMVs with $10 \leq \varepsilon < 20$m s^{-1}.

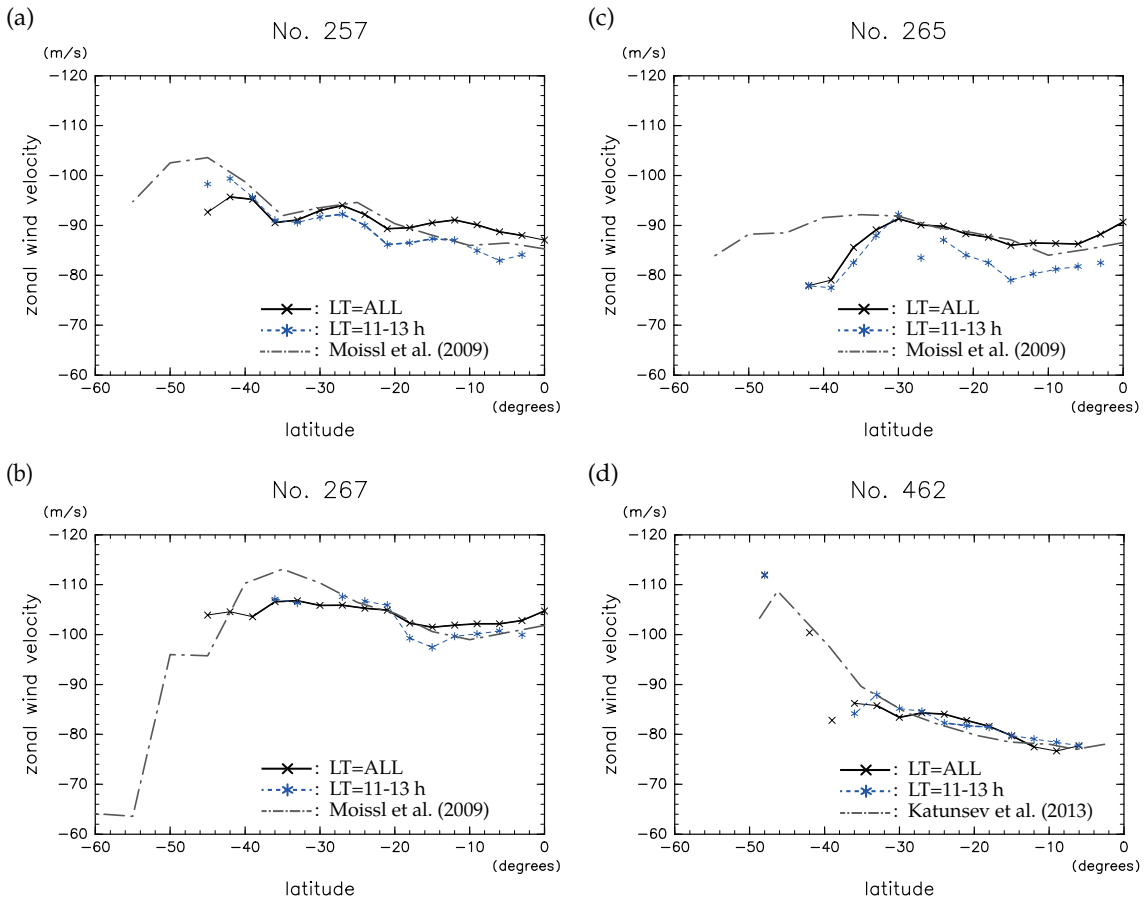

Figure 5.2: Mean zonal winds compared with previous studies for the orbits (a) 257, (b) 265, (c) 267 and (d) 462. Cross marks connected by solid lines show the zonal winds averaged longitudinally using the all CMVs for each latitude (here, a cross mark is shown if the number of CMVs obtained at a latitudinal grid point is greater than or equal to three. Thick (thin) lines are drawn between adjacent grid points if the numbers of CMVs are greater than or equal to ten (three) at both ends). Asterisks and dashed lines: as cross marks and solid lines, respectively, but for the average limiting the local time between 11 am and 13 pm. Dash-dotted lines show the zonal mean zonal winds reported by previous studies: (a–c) *Moissl et al.* (2009) and (d) *Khatuntsev et al.* (2013). These results are obtained with manual tracking.

Moissl et al. (2009) and *Khatuntsev et al.* (2013) showed zonal mean zonal winds obtained manually with CMV for some orbits, and comparison with our results are available for the orbits 257, 265, 267 and 462 as shown in Fig. 5.2. Since the longitudinal coverage of their CMVs are unknown, we show two type of means for comparison. One is the mean over longitudinal ranges corresponding to the local time between 11 am and 13 pm as shown by blue lines in Fig. 5.1, and the other is over the entire longitudinal range shown in Fig. 5.1. Given the coverage uncertainty, we consider that our results agrees well with the previous studies. *Moissl et al.* (2009) pointed out a large change of zonal winds by about 20 m s^{-1} over two days from the orbit (day) 265 to the orbit 267, and they argued that it is likely an actual change. Our result supports it.

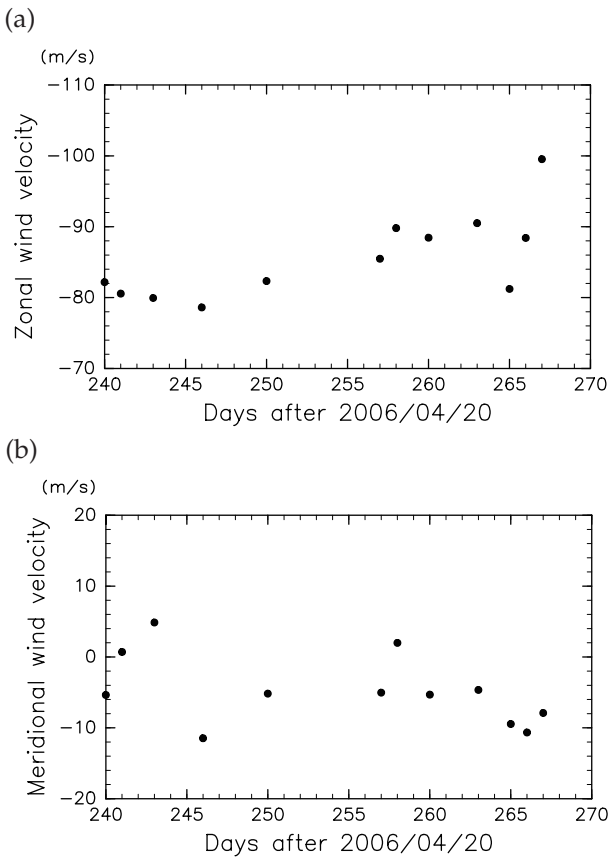

Figure 5.3: Mean (a) zonal and (b) meridional winds for the twelve orbits in the period 2 obtained by averaging CMVs between 20°S and the equator. The abscissa is the orbit numbers, which are the days after April 20, 2006.

Figure 5.1 suggests large-scale orbit-to-orbit variability both in zonal and meridional winds. Figure 5.3 shows mean winds averaged horizontally between 20°S and the equator. The low-latitudinal mean winds fluctuate day by day. There is no clear relationship between the zonal and meridional winds, and they do not appear to exhibit simple periodicities. This result suggests that the large-scale wind filed is not dominated by a single planetary-scale wave. Also, F averaged over the same region is not correlated with the mean zonal or meridional winds (figure not shown). This is the case for the period 3.

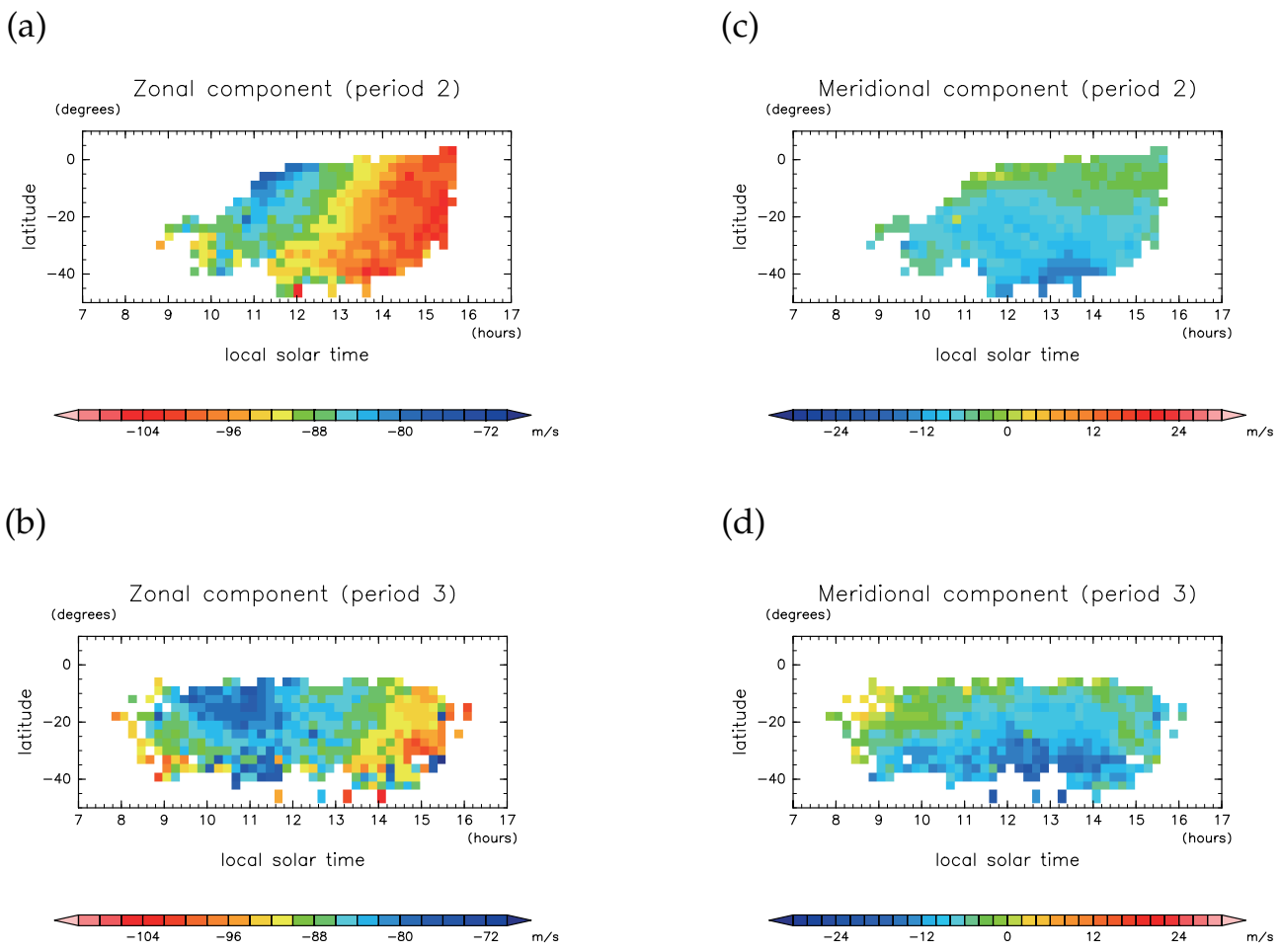

Figure 5.4: Tidal component obtained for the periods 2 (a, c) and 3 (b, d). (a, b) Zonal wind; (c,d) meridional wind. The results are shown where the number of CMVs is greater than or equal to 4.

The CMVs are averaged over time for each of the periods 2 and 3 as functions of local time and latitude (Fig. 5.4). The mean zonal wind is slower in the period 3 than in the period 2 as shown by *Kouyama et al.* (2013a). The horizontal distribution of zonal and meridional winds are consistent with the structure of thermal tides shown by *Moissl et al.* (2009) and *Khatuntsev et al.* (2013). Namely, the zonal wind is maximized (wind speed minimized) around 11 am, which is closer to the result by *Moissl et al.* (2009) who used periods close to ours; the meridional wind slightly away from the equator is minimized (wind speed maximized) at around 13 pm as shown by *Khatuntsev et al.* (2013) (*Moissl et al.*, 2009 did not show the meridional wind result). These results are roughly consist with the numerical results of thermal tide by *Takagi and Matsuda* (2005).

Many of the horizontal distributions of CMVs for individual orbits in Fig. 5.1 exhibit similar features as the tidal features shown in Fig. 5.4. However, there are some differences in the large-scale features among the orbits. Also, CMVs have small-scale features as discussed for the orbit 246 in Section 3.6. To investigate these features is left for a future study, since close scrutiny of data quality is desired to ensure the robustness of results.

Chapter 6

Summary and conclusions

We have examined the problems of digital cloud tracking and proposed a new method suitable for dayside UV images of the cloud deck of Venus. The version 2.0 product of the Venus Monitoring Camera onboard the Venus Express has been analyzed with this method.

Conventional digital cloud tracking based on cross-correlation fails often. This is primarily because the cross-correlation between the template and target sub-images can be maximized by a false match among distant portions of cloud deck.

The proposed cloud tracking method uses multiple images obtained successively over a few hours. Cross-correlations are computed from the pair combinations of the images and are superposed on the coordinates with respect to horizontal velocities. It was shown that this superposition lowers the correlation peaks associated with false matches. Thus, the failure is reduced. It is also expected that the superposition improves the accuracy of CMVs.

Spatial moving average of the cross-correlation surfaces can further improve the accuracy at the expense of horizontal resolution (the STS estimation). This procedure is optional, but it was used in most cases shown in this paper.

We propose two methods to evaluate the precision and error of each CMV. One of them relies on the confidence bounds of cross-correlation, where the anisotropy of clouds and the effective degrees of freedom are taken into account. Although its result does not show the confidence bounds of CMVs, it gives a relative measure of their precision termed ε. This method is applicable to the conventional cloud tracking based on a single pair of images. The other method relies on the comparison of two independent CMV estimates obtained by separating the successive images into two groups. This method provides a more direct estimate of error in CMVs, which is termed χ. These two evaluations can be combined to screen CMVs. We applied the threshold values $\varepsilon = 20$ m s^{-1} and $\chi = 10$ m s^{-1}.

Typical values of χ and ε obtained in this study are 2 and 8 m s^{-1} at low latitude and 2–3 and 14 m s^{-1} at mid

latitude, respectively. Visual inspection suggested that ε tends to be consistent with subjective impression of the ambiguity on CMVs, so it can be a measure of ambiguity of manual tracking, not only ambiguity of digital tracking. This is because ε is dependent on morphology and indicates the range (in m s^{-1}) over which cross-correlations are statistically indistinguishable. On the other hand, χ is a measure of consistency among the images used to derive a CMV. The fact that χ is generally better than ε indicates that digital tracking can be more precise by the superposition of cross-correlation than manual tracking. However, there are factors such as cloud deformation that degrade CMVs and may not be reflected in χ as shown in Section 4.4. Therefore, the error of our CMVs can be greater than χ.

It was shown that the spatial moving average of correlation surfaces actually reduces errors. Also, the optical correction and the limb fitting applied in our preprocess were shown to be effective.

CMVs obtained in this study were investigated and compared with previous studies. Our results are consistent with previous studies obtained by manual tracking. The results supports the existence of day-to-day variability of large-scale winds on the order of $\mathcal{O}(10)$ m s^{-1}. They further suggest smaller-scale features at $\mathcal{O}(1000)$ km; a further study is ongoing to investigate them.

It was found that erroneous CMVs sometimes elude the screening, especially at mid latitude. It may be useful to additionally adapt the traditional screening based on the comparison of neighboring vectors. Also, it may be worth exploring to change the template size possibly depending on latitude.

Our method is expected to advance the study of the atmosphere of Venus. It is planned to use it to process the images to be obtained by Japan's Venus orbiter Akatsuki.

Appendix A

Estimation of the effective degrees of freedom

The effective degrees of freedom of the superposed cross-correlation is for formulated in this section. The effective degrees of freedom of a simple cross-correlation, which is used in the tracking based on a single image pair, can be expressed by a standard formula (e.g., *Thomson and Emery*, 1994) as

$$M_e^{(1)} = \frac{M}{\Omega^{(1)}}, \tag{A.1}$$

$$\Omega^{(1)} = \sum_{\tau=-M}^{M} \left(1 - \frac{|\tau|}{M}\right) R_{xx}(\tau) R_{yy}(\tau), \tag{A.2}$$

where M is the number of pixels, x and y represent the sequences between which cross correlation is computed, and R_{xx} and R_{yy} are their auto correlations with the lag equal to τ:

$$R_{xx}(\tau) = \frac{M}{M-|\tau|} \frac{\sum_{\omega=1}^{M-|\tau|} x'(\omega) x'(\omega+|\tau|)}{\sum_{\omega=1}^{M} x'(\omega)^2}, \tag{A.3}$$

$$R_{yy}(\tau) = \frac{M}{M-|\tau|} \frac{\sum_{\omega=1}^{M-|\tau|} y'(\omega) y'(\omega+|\tau|)}{\sum_{\omega=1}^{M} y'(\omega)^2}, \tag{A.4}$$

where dash represents the deviation from the sample mean. In our problem, x and y are one-dimensionalized brightness sequences from sub-regions, so $M = IJ = 48^2 = 2304$. The effective degree of freedom is evaluated for

the combination of the template and target regions that maximize the cross-correlation. Thus, x and y are similar, and R_{xx} and R_{yy} have similar values. Eq. (A.2) is suitable to estimate $\Omega^{(1)}$ for such a case.

We define the effective degree of freedom for the superposed cross-correlation Eq. (3.15) as

$$M_e \equiv \frac{PM}{\Omega}, \tag{A.5}$$

$$\Omega \equiv \frac{1}{P}\sum_{p=1}^{P}\Omega^{(p)}, \tag{A.6}$$

where $\Omega^{(p)}$ is the correlation length obtained from the p-th pair of images by using Eq. (A.2). Eqs. (A.5) and (A.6) are justified by using Eqs. (A.1) and (A.2) as follows. The superposed cross-correlation r of Eq. (3.15) can be rewritten as

$$r = \frac{1}{p}\sum_{p=1}^{P} r_p = \frac{1}{P}\sum_{p=1}^{P}\frac{\mathrm{Cov}(x^{(p)}, y^{(p)})}{\sigma_{x^{(p)}}\sigma_{y^{(p)}}}, \tag{A.7}$$

where Cov and σ represent covariance and standard deviation, and $x^{(p)}$ and $y^{(p)}$ represent the brightness sequence of template and target subimages of the p-th pair. If $\sigma_{x^{(p)}}$ and $\sigma_{y^{(p)}}$ can be approximated by a common constant σ (Approximation A), the r of Eq. (A.7) is approximated as

$$r \simeq \frac{1}{\sigma^2 P}\sum_{p=1}^{P}\mathrm{Cov}(x^{(p)}, y^{(p)}) = \frac{1}{\sigma^2}\frac{1}{PM}\sum_{t=1}^{PM} X_t Y_t, \tag{A.8}$$

where X_t and Y_t $(t = 1, 2, \cdots, PM)$ represent concatenated brightness sequences over the P pairs. In this case, the correlation length is written as

$$\Omega_c \equiv \sum_{\tau=-PM}^{PM}\left(1 - \frac{|\tau|}{PM}\right) R_{XX}(\tau) R_{YY}(\tau), \tag{A.9}$$

from Eq. (A.2), and the effective degree of freedom is expressed as PM/Ω_c, since the data length is PM. Since Approximation A is expected to be valid, Ω and Ω_c are expected to have similar values. Therefore, Eqs. (A.5) and (A.6) are valid, which justifies Eqs. (A.5) and (A.6).

Appendix B

Elliptic paraboloid and parabola fitting

B.1 Elliptic paraboloid fitting (two-dimensional)

To compute the precision measure ε_{1u} and ε_{1v} the correlation surface is fitted by a quadratic surface

$$r(u,v) \equiv Au^2 + 2Buv + Cv^2 + 2Du + 2Ev + F, \tag{B.1}$$

by using the least square fitting. The fitted surface is an elliptic paraboloid if $AC - B^2 > 0$, and it has a maximum if $A < 0$. Then, the center (u_c, v_c), the semi-major axis R_1, and its angle θ, of the ellipse $r(u,v) = r_{\rm lb}$ are expressed as

$$u_c = \frac{CD - BE}{B^2 - AC}, \tag{B.2}$$

$$v_c = \frac{AE - BD}{B^2 - AC}, \tag{B.3}$$

$$\theta = \frac{1}{2}\arctan\left(\frac{2B}{A-C}\right), \tag{B.4}$$

$$R_1 = \max(\hat{R_1}, \hat{R_2}), \tag{B.5}$$

$$\hat{R_1} \equiv \sqrt{\left\{(u_c\cos\theta + v_c\sin\theta)^2 - \frac{F'}{A}\cos^2\theta\right\} - \left\{(-u_c\sin\theta + v_c\cos\theta)^2 - \frac{F'}{A}\sin^2\theta\right\}\frac{A\sin^2\theta - C\cos^2\theta}{A\cos^2\theta - C\sin^2\theta}}, \tag{B.6}$$

$$\hat{R_2} \equiv \sqrt{\left\{(-u_c\sin\theta + v_c\cos\theta)^2 - \frac{F'}{A}\sin^2\theta\right\} - \left\{(u_c\cos\theta + v_c\sin\theta)^2 - \frac{F'}{A}\cos^2\theta\right\}\frac{A\cos^2\theta - C\sin^2\theta}{A\sin^2\theta - C\cos^2\theta}}, \tag{B.7}$$

$$F' \equiv F - r_{\rm lb}. \tag{B.8}$$

Here, u and v are horizontal velocities.

We conducted the fitting, nevertheless, on the pixel coordinates proportional to longitude and latitude. Since they are anisotropic in the velocity coordinates if not at the equator, the result does not strictly follow Eqs. (B.4) and (B.5). However, the discrepancy is only significant when $\hat{R_1} \simeq \hat{R_2}$, and such cases are covered by ε_{2u} and ε_{2v}.

Therefore, our practical choice is not harmful.

B.2 Quadratic function (one-dimensional)

If $r(u,v)$ is peaked at $(u_{\max}, v_{\max})$, the precision measure ε_{2u} is obtained by fitting $r(u, v_{\max}) - r_{\mathrm{lb}}$, a function of u, by

$$f(u) = c_0(u-u_c)^2 + r_{\max}, \tag{B.9}$$

by using the least square method. Then, ε_{2u} is expressed as

$$\varepsilon_{2u} = \pm\sqrt{\frac{r_{\max}-r_{\mathrm{lb}}}{-c_0}} \tag{B.10}$$

when c_0 is negative; ε_{2u} is set to infinity if $c_0 \geq 0$. Similarly, ε_{2v} is obtained by fitting the cross section at $u = u_{\max}$, $r(u_{\max}, v)$, by

$$g(v) = c_1(v-v_c)^2 + r_{\max}. \tag{B.11}$$

Then, ε_{2v} is expressed as

$$\varepsilon_{2v} = \pm\sqrt{\frac{r_{\max}-r_{\mathrm{lb}}}{-c_1}} \tag{B.12}$$

when c_1 is negative.

Appendix C

Sensitivity experiment

In this section, we will investigate the relationship between template size as mentioned in Section 4.3 and high-pass processing, and the dependence on template size in cloud tracking. Here, we have looked at the consistency of two wind vector fields estimated from brightness distributions, with and without preprocessing, in previous studies that have examined the differences in the estimation results (*Rossow et al.*, 1990). *Rossow et al.* (1990) used a scheme which had high-pass processing[1] applied at the same resolution as the template size, and one which had no high-pass processing at all. As a result, a significant difference in the estimated results, depending on whether or not there is preprocessing, was reported. However, high-pass filtering for the brightness for the template and search region has already been applied when the cross-correlational method is used, as indicated clearly by Eq. (3.9). That is to say, the cross-correlation method involves high-pass processing by calculating the running mean. Consequently, the fact that there is a significant difference between the results from the two schemes seems contradictory. Based on these points, we will use the cloud tracking method and statical precision evaluation criteria developed in this study, to conduct sensitivity experiments regarding the relationship between the two estimated results. The sensitivity experiments will involve estimating the wind based on the conditions below, and investigate whether there is a significant difference between them.

- In sensitivity experiment 1, a brightness distribution for which high-pass processing with the same resolution as a $6^\circ \times 6^\circ$ template has been applied, and a brightness distribution in which no high-pass processing has been applied are used, and the difference in the estimated results is compared.

- In sensitivity experiment 2, a brightness distribution for which high-pass processing with the same resolution as a $4^\circ \times 4^\circ$ template has been applied, and a brightness distribution in which no high-pass processing has been applied are used, and the difference in the estimated results is compared. The template size in the former case is $4^\circ \times 4^\circ$ and in the latter case is $6^\circ \times 6^\circ$.

[1] The cross-correlation method involves obtaining the running mean for high-pass processing (at the same resolution as the template size) of the brightness distribution, and determining its difference from the original brightness distribution. A 2D Rectangular window is used for the running mean, so that the weights at each grid points are equal.

- In sensitivity experiment 3, the differences between sensitivity experiment 1 and sensitivity experiment 2 are compared. In other words, the difference due to filter size is examined.

Regardless of the fact that the filter size used in sensitivity experiment 1 is slightly smaller than the template size, there is good agreement between the two wind fields at low latitudes (10°N–30°S) which satisfy $\varepsilon < 10$ m s^{-1} in Fig. 5.1, in Fig. C.1 (a) and (d). From this, we see that when deciding on a specific template size, we are applying high-pass processing at the same scale. In rare instances however, there are regions where the wind is slightly increased when there is a streaked pattern present. This is strikingly evident when comparing sensitivity experiments 1 and 2. That is to say, in regions where there is a large difference in zonal and meridional wind in the two experiments (Fig. 5.1 (a, d) and (b, e)), the differences can generally be seen along the streaks. Hence, there is a trend that the difference in zonal wind (b, e) in sensitivity experiment 2, in which the tracking pattern was finer, is even greater than the zonal wind in sensitivity experiment 1 (Fig. 5.1 (a, d)). This is the same trend as for $r_{\max}$ in sensitivity experiments 1 and 2 (j, k); at $r_{\max}$, this result is even more noteworthy. As a result, ε based on the confidence interval for $r_{\max}$ results in a reduction in the template size leading to lower accuracy (g, h). However, at low latitudes, the differences between winds are small, and the difficulty in assessing if there is a significant difference between the two results is evident even in the results of sensitivity experiment 3 (c, f, i, l). To put this another way, if we consider that there is no improvement in the estimation results with the filter size, then we cannot assign merits, in terms of which of the results are more accurate. Therefore, when estimating the wind field with cloud tracking schemes, we would want to use a $6° \times 6°$ resolution, because the noise is smaller.

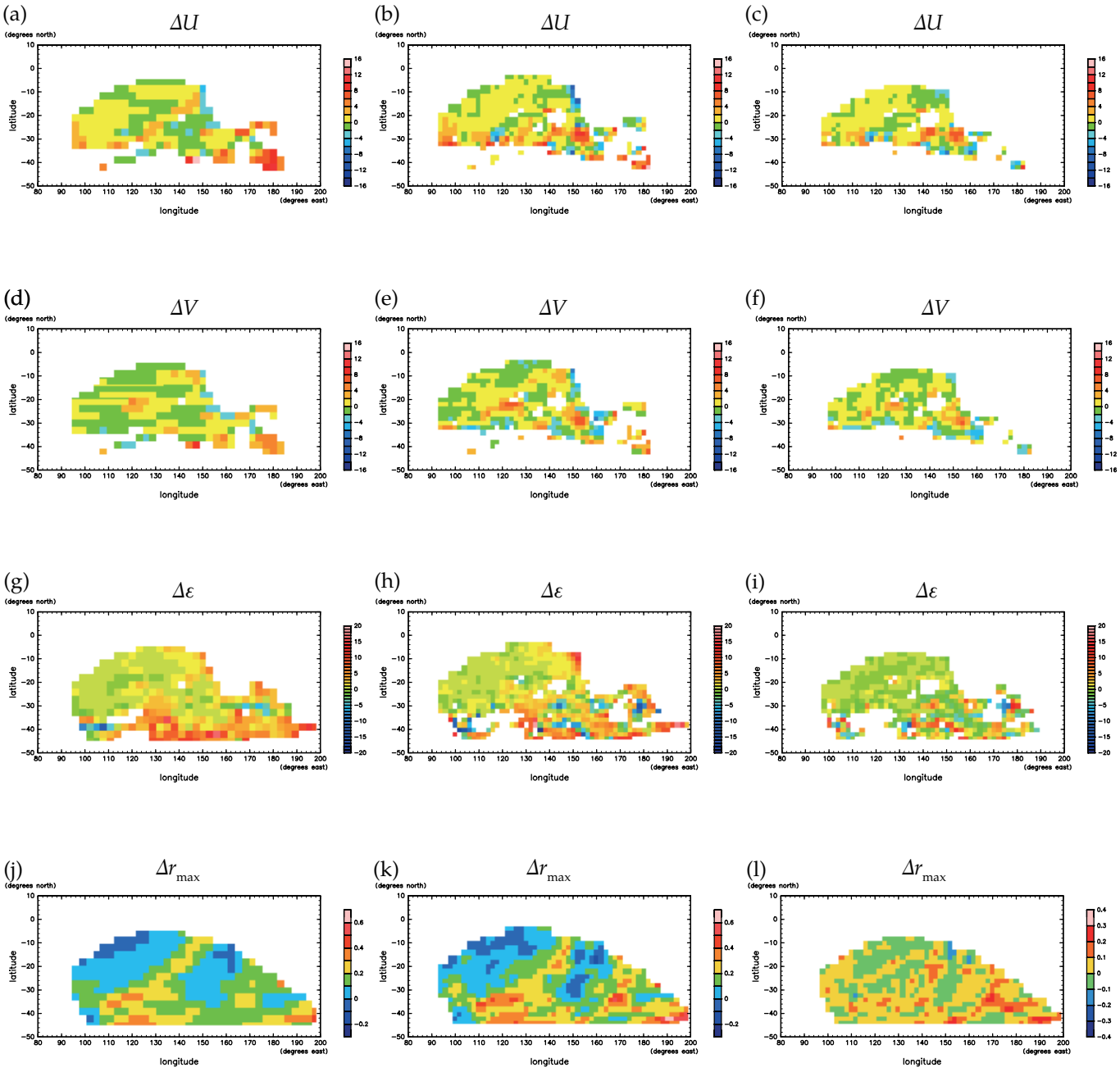

Figure C.1: This shows the results of sensitivity experiments 1 to 3 for orbit 246. The left column (a, d, g, j) shows the difference in zonal and meridional wind, ε and $r_{\max}$ in sensitivity experiment 1. The middle column (b, e, h, k) corresponds to the same physical and statistical quantities as (a, d, g, j) for sensitivity experiment 2. The right column (c, f, i, l) corresponds to the physical and statistical quantities derived for (b, e, h, k) based on (a, d, g, j) for sensitivity experiment 3.

Acknowledgements

The author would like to express his sincere gratitude to Prof. Takeshi Horinouchi of the University of Hokkaido for his elaborated guidance, considerable encouragement and invaluable discussion that make my research of great achievement and my study life unforgettable. The author expresses his gratitude to the referee professors; Prof. Atsushi Kubokawa and Prof. Masatomo Fujiwara of the University of Hokkaido and Prof. Takeshi Imamura of the Institute of Space and Astronautical Science (ISAS) of Japan Aerospace Exploration Agency (JAXA) for advice and comments in this study.

The author also thank Drs. Kazunori Ogohara of the University of Siga prefecture, Toru Kouyama of National Institute of Advanced Industrial Science and Technology (AIST), and Takeshi Imamura of ISAS/JAXA for their valuable comments. The program used for the preprocessing (Section 3.1) was developed and provided by Drs. Kazunori Ogohara of the University of Siga prefecture, Toru Kouyama of AIST, Hiroki Yamamoto of Japan Agency for Marine-Earth Science and Technology, Naoki Sato of Tokyo Gakugei University, Masahiro Takagi of Kyoto Sangyo University, and Takeshi Imamura of ISAS/JAXA. We used the Akatsuki L2 program developed by Dr. Manabu Yamada of Chiba Institute of Technology and collaborators and the SPICE toolkit provided by NASA (http://naif.jpl.nasa.gov/naif/). The VEX/VMC data was obtained from ESA's FTP server (ftp://psa.esac.esa.int/pub/mirror/VENUS-EXPRESS/VMC). The author thank ESA and the VEX project for conducting observations and for freely providing valuable data.

This study was supported in part by the Grant-in-Aid for the IFES-GCOE Global COE Program on "Establishment of Center for Integrated Field Environmental Science" at the University of Hokkaido.

Bibliography

Avduevskiy, V., M. Marov, Y. Kulikov, V. Shari, A. Gorbachevskiy, G. Uspenskiy, and Z. Cheremukhina (1983), STRUCTURE AND PARAMETERS OF THE VENUS ATMOSPHERE ACCORDING TO VENERA PROBE DATA, *Venus*, p. 280.

Belton, M. J., P. J. Gierasch, M. D. Smith, P. Helfenstein, P. J. Schinder, J. B. Pollack, K. A. Rages, A. P. Ingersoll, K. P. Klaasen, J. Veverka, et al. (1991), Images from Galileo of the Venus cloud deck, *Science*, *253*(5027), 1531–1536, doi:10.1126/science.253.5027.1531.

Boyer, C., and P. Guérin (1969), Etude de la rotation rétrograde, en 4 jours, de la couche extérieure nuageuse de Vénus, *Icarus*, *11*(3), 338–355, doi:10.1016/0019-1035(69)90067-0.

Carlson, R. o., K. Baines, T. Encrenaz, F. Taylor, P. Drossart, L. Kamp, J. Pollack, E. Lellouch, A. Collard, S. Calcutt, et al. (1991), Galileo infrared imaging spectroscopy measurements at Venus, *Science*, *253*(5027), 1541–1548.

Davies, M. E., T. R. Colvin, P. G. Rogers, P. Chodas, W. Sjogren, E. Akim, V. Stepanyantz, Z. Vlasova, and A. Zakharov (1992), The rotation period, direction of the north pole, and geodetic control network of Venus, *Journal of Geophysical Research: Planets (1991–2012)*, *97*(E8), 13,141–13,151, doi:10.1029/92JE01166.

Del Genio, A. D., and W. B. Rossow (1990), Planetary-scale waves and the cyclic nature of cloud top dynamics on Venus, *Journal of the Atmospheric Sciences*, *47*(3), 293–318, doi:10.1175/1520-0469(1990)047<0293:PSWATC>2.0.CO;2.

Esposito, L. W., J.-L. Bertaux, V. Krasnopolsky, V. Moroz, and L. Zasova (1997), Chemistry of lower atmosphere and clouds, *Venus II*, pp. 415–458.

Fegley Jr, B., G. Klingelhöfer, K. Lodders, and T. Widemann (1997), Geochemistry of surface-atmosphere interactions on Venus, in *Venus II: Geology, Geophysics, Atmosphere, and Solar Wind Environment*, vol. 1, p. 591.

Fels, S. B., and R. S. Lindzen (1974), The interaction of thermally excited gravity waves with mean flows, *Geophysical and Astrophysical Fluid Dynamics*, *6*(2), 149–191, doi:10.1080/03091927409365793.

Fisher, R. A. (1915), Frequency distribution of the values of the correlation coefficient in samples from an indefinitely large population, *Biometrika*, pp. 507–521, doi:10.2307/2331838.

Gierasch, P. J. (1975), Meridional circulation and the maintenance of the Venus atmospheric rotation, *Journal of the Atmospheric Sciences*, *32*(6), 1038–1044, doi:10.1175/1520-0469(1975)032<1038:MCATMO>2.0.CO;2.

Holmlund, K. (1998), The utilization of statistical properties of satellite-derived atmospheric motion vectors to derive quality indicators, *Weather and Forecasting*, *13*(4), 1093–1104, doi:10.1175/1520-0434(1998)013<1093:TUOSPO>2.0.CO;2.

Hubbard, W., B. Sicardy, R. Miles, A. Hollis, R. Forrest, I. Nicolson, G. Appleby, W. Beisker, C. Bittner, H.-J. Bode, et al. (1993), The occultation of 28 Sgr by Titan, *Astronomy and Astrophysics*, *269*, 541–563, doi:10.1006/icar.1993.1067.

Hueso, R., J. Peralta, I. Garate-Lopez, T. Bandos, and A. Sánchez-Lavega (2015), Six years of venus winds at the upper cloud level from uv, visible and near infrared observations from virtis on venus express, *Planetary and Space Science*, *113*, 78–99.

Hunten, D. M. (1983), *Venus*, University of Arizona Press.

Iga, S., and Y. Matsuda (1999), A Mechanism of the super-rotation in the Venus atmosphere: Meridional circulation and barotropic instability, *Theoretical and Applied Mechanics*, *48*, 379–383.

Kawabata, K. (1987), Remote sensing of aerosols in the planetary atmosphere (in japanese), *Meteorol. Soc. of Jpn*, *155*, 1–34.

Khatuntsev, I., M. Patsaeva, D. Titov, N. Ignatiev, A. Turin, S. Limaye, W. Markiewicz, M. Almeida, T. Roatsch, and R. Moissl (2013), Cloud level winds from the Venus Express Monitoring Camera imaging, *Icarus*, *226*(1), 140–158, doi:10.1016/j.icarus.2013.05.018.

Kliore, A. J., and I. R. Patel (1980), Vertical structure of the atmosphere of Venus from Pioneer Venus orbiter radio occultations, *Journal of Geophysical Research: Space Physics (1978–2012)*, *85*(A13), 7957–7962, doi:10.1029/JA085iA13p07957.

Kliore, A. J., and I. R. Patel (1982), Thermal structure of the atmosphere of Venus from Pioneer Venus radio occultations, *Icarus*, *52*(2), 320–334, doi:10.1016/0019-1035(82)90115-4.

Knollenberg, R., and D. Hunten (1980), The microphysics of the clouds of venus: Results of the pioneer venus particle size spectrometer experiment, *Journal of Geophysical Research: Space Physics*, *85*(A13), 8039–8058.

Kouyama, T., T. Imamura, M. Nakamura, T. Satoh, and Y. Futaana (2012), Horizontal structure of planetary-scale waves at the cloud top of Venus deduced from Galileo SSI images with an improved cloud-tracking technique, *Planetary and Space Science*, *60*(1), 207–216, doi:10.1016/j.pss.2011.08.008.

Kouyama, T., T. Imamura, M. Nakamura, T. Satoh, and Y. Futaana (2013a), Long-term variation in the cloud-tracked zonal velocities at the cloud top of Venus deduced from Venus Express VMC images, *Journal of Geophysical Research: Planets*, *118*(1), 37–46, doi:10.1029/2011JE004013.

Kouyama, T., A. Yamazaki, M. Yamada, and T. Imamura (2013b), A method to estimate optical distortion using planetary images, *Planetary and Space Science*, *86*, 86–90, doi:10.1016/j.pss.2013.06.027.

Limaye, S. S. (2007), Venus atmospheric circulation: Known and unknown, *Journal of Geophysical Research: Planets (1991–2012)*, *112*(E4), doi:10.1016/0273-1177(90)90170-5.

Limaye, S. S., and V. E. Suomi (1981), Cloud motions on Venus: Global structure and organization, *Journal of the Atmospheric Sciences*, *38*(6), 1220–1235, doi:10.1175/1520-0469(1981)038<1220:CMOVGS>2.0.CO;2.

Limaye, S. S., C. J. Grund, and S. P. Burre (1982), Zonal mean circulation at the cloud level on Venus: Spring and Fall 1979 OCPP observations, *Icarus*, *51*(2), 416–439, doi:10.1016/0019-1035(82)90092-6.

Limaye, S. S., C. Grassotti, and M. J. Kuetemeyer (1988), Venus: Cloud level circulation during 1982 as determined from pioneer cloud photopolarimeter images: I. Time and zonally averaged circulation, *Icarus*, *73*(2), 193–211, doi:10.1016/0019-1035(88)90093-0.

Limaye, S. S., W. Markiewicz, R. Krauss, N. Ignatiev, T. Roatsch, and K. Matz (2015), Focal lengths of Venus Monitoring Camera from limb locations, *Planetary and Space Science*, doi:10.1016/j.pss.2015.01.010.

Markiewicz, W., D. Titov, N. Ignatiev, H. Keller, D. Crisp, S. Limaye, R. Jaumann, R. Moissl, N. Thomas, L. Esposito, et al. (2007), Venus monitoring camera for Venus Express, *Planetary and Space Science*, *55*(12), 1701–1711, doi:10.1016/j.pss.2007.01.004.

Matsuda, Y. (2000), *Planetary Meteorology (in Japanese)*, University of Tokyo Press.

Matsuda, Y. (2011), *Introduction to Planetary Meteorology (in Japanese)*, Iwanami Shoten.

Migliorini, A., D. Grassi, L. Montabone, S. Lebonnois, P. Drossart, and G. Piccioni (2012), Investigation of air temperature on the nightside of Venus derived from VIRTIS-H on board Venus-Express, *Icarus*, *217*(2), 640–647, doi:10.1016/j.icarus.2011.07.013.

Moissl, R., I. Khatuntsev, S. Limaye, D. Titov, W. Markiewicz, N. Ignatiev, T. Roatsch, K.-D. Matz, R. Jaumann, M. Almeida, et al. (2009), Venus cloud top winds from tracking UV features in Venus Monitoring Camera images, *Journal of Geophysical Research: Planets (1991–2012)*, *114*(E5), doi:10.1029/2008JE003117.

Newman, M., and C. Leovy (1992), Maintenance of strong rotational winds in Venus' middle atmosphere by thermal tides, *Science*, *257*(5070), 647–650, doi:10.1126/science.257.5070.647.

Newman, M., G. Schubert, A. J. Kliore, and I. R. Patel (1984), Zonal winds in the middle atmosphere of Venus from Pioneer Venus radio occultation data, *Journal of the atmospheric sciences*, *41*(12), 1901–1913.

Ogohara, K., T. Kouyama, H. Yamamoto, N. Sato, M. Takagi, and T. Imamura (2012), Automated cloud tracking system for the Akatsuki Venus Climate Orbiter data, *Icarus*, *217*(2), 661–668, doi:10.1016/j.icarus.2011.05.017.

Peralta, J., R. Hueso, and A. Sánchez-Lavega (2007), A reanalysis of Venus winds at two cloud levels from Galileo SSI images, *Icarus*, *190*(2), 469–477, doi:10.1016/j.icarus.2007.03.028.

Piccialli, A., S. Tellmann, D. Titov, S. Limaye, I. Khatuntsev, M. Pätzold, and B. Häusler (2012), Dynamical properties of the Venus mesosphere from the radio-occultation experiment VeRa onboard Venus Express, *Icarus*, *217*(2), 669–681, doi:10.1016/j.icarus.2011.07.016.

Rossow, W. B., and G. P. Williams (1979), Large-scale motion in the Venus stratosphere, *Journal of the Atmospheric Sciences*, *36*(3), 377–389, doi:10.1175/1520-0469(1979)036<0377:LSMITV>2.0.CO;2.

Rossow, W. B., A. D. Del Genio, and T. Eichler (1990), Cloud-tracked winds from Pioneer Venus OCPP images, *Journal of the Atmospheric Sciences*, *47*(17), 2053–2084, doi:10.1175/1520-0469(1990)047<2053:CTWFVO>2.0.CO;2.

Sánchez-Lavega, A., R. Hueso, G. Piccioni, P. Drossart, J. Peralta, S. Pérez-Hoyos, C. F. Wilson, F. W. Taylor, K. H. Baines, D. Luz, et al. (2008), Variable winds on Venus mapped in three dimensions, *Geophysical Research Letters*, *35*(13), doi:10.1029/2008GL033817.

Schubert, G., C. Covey, A. D. Genio, L. Elson, G. Keating, A. Seiff, R. Young, J. Apt, C. Counselman, A. Kliore, et al. (1980), Structure and circulation of the Venus atmosphere, *Journal of Geophysical Research: Space Physics (1978–2012)*, *85*(A13), 8007–8025, doi:10.1029/JA085iA13p08007.

Sciacchitano, A., F. Scarano, and B. Wieneke (2012), Multi-frame pyramid correlation for time-resolved PIV, *Experiments in fluids*, *53*(4), 1087–1105, doi:10.1007/s00348-012-1345-x.

Seiff, A. (1983), THERMAL STRUCTURE OF THE ATMOSPHERE OF VENUS, *Venus*, p. 215.

Seiff, A., J. Schofield, A. Kliore, F. Taylor, S. Limaye, H. Revercomb, L. Sromovsky, V. Kerzhanovich, V. Moroz, and M. Y. Marov (1985), Models of the structure of the atmosphere of Venus from the surface to 100 kilometers altitude, *Advances in Space Research*, *5*(11), 3–58, doi:10.1016/0273-1177(85)90197-8.

Shapiro, I., J. Chandler, D. Campbell, A. Hine, and N. Stacy (1990), The spin vector of venus, *The Astronomical Journal*, *100*, 1363–1368.

Sobolev, V. V. (1975), Light scattering in planetary atmospheres, *(Translation of Rasseianie sveta v atmosferakh planet, Moscow, Izdatel'stvo Nauka, 1972.) Oxford and New York, Pergamon Press (International Series of Monographs in Natural Philosophy. Volume 76), 1975. 263 p., 1.*

Svedhem, H., D. Titov, D. McCoy, J.-P. Lebreton, S. Barabash, J.-L. Bertaux, P. Drossart, V. Formisano, B. Häusler, O. Korablev, et al. (2007), Venus Express—the first European mission to Venus, *Planetary and Space Science*, *55*(12), 1636–1652.

Takagi, M., and Y. Matsuda (2005), Sensitivity of thermal tides in the Venus atmosphere to basic zonal flow and newtonian cooling, *Geophysical research letters*, *32*(2), doi:10.1029/2004GL022060.

Takagi, M., and Y. Matsuda (2007), Effects of thermal tides on the Venus atmospheric superrotation, *Journal of Geophysical Research: Atmospheres (1984–2012)*, *112*(D9), doi:10.1029/2006JD007901.

Thomson, R. E., and W. J. Emery (1994), *Data analysis methods in physical oceanography*, Pergamon.

Titov, D. V., W. J. Markiewicz, N. I. Ignatiev, L. Song, S. S. Limaye, A. Sanchez-Lavega, J. Hesemann, M. Almeida, T. Roatsch, K.-D. Matz, et al. (2012), Morphology of the cloud tops as observed by the Venus Express Monitoring Camera, *Icarus*, *217*(2), 682–701, doi:10.1016/j.icarus.2011.06.020.

Yamamoto, M., and M. Takahashi (2003a), The Fully Developed Superrotation Simulated by a General Circulation model of a Venus-like Atmosphere, *Journal of the atmospheric sciences*, *60*(3), 561–574, doi:10.1175/1520-0469(2003)060<0561:TFDSSB>2.0.CO;2.

Yamamoto, M., and M. Takahashi (2003b), Superrotation and equatorial waves in a T21 Venus-like AGCM, *Geophysical research letters*, *30*(9), doi:10.1029/2003GL016924.